

Hybrid apparatus for Bose-Einstein condensation and cavity quantum electrodynamics: Single atom detection in quantum degenerate gases

Anton Öttl, Stephan Ritter, Michael Köhl,* and Tilman Esslinger
Institute of Quantum Electronics, ETH Zurich, 8093 Zurich, Switzerland
 (Dated: 18th October 2018)

We present and characterize an experimental system in which we achieve the integration of an ultrahigh finesse optical cavity with a Bose-Einstein condensate (BEC). The conceptually novel design of the apparatus for the production of BECs features nested vacuum chambers and an *in vacuo* magnetic transport configuration. It grants large scale spatial access to the BEC for samples and probes via a modular and exchangeable “science platform.” We are able to produce ^{87}Rb condensates of 5×10^6 atoms and to output couple continuous atom lasers. The cavity is mounted on the science platform on top of a vibration isolation system. The optical cavity works in the strong coupling regime of cavity quantum electrodynamics and serves as a quantum optical detector for single atoms. This system enables us to study atom optics on a single particle level and to further develop the field of quantum atom optics. We describe the technological modules and the operation of the combined BEC cavity apparatus. Its performance is characterized by single atom detection measurements for thermal and quantum degenerate atomic beams. The atom laser provides a fast and controllable supply of atoms coupling with the cavity mode and allows for an efficient study of atom field interactions in the strong coupling regime. Moreover, the high detection efficiency for quantum degenerate atoms distinguishes the cavity as a sensitive and weakly invasive probe for cold atomic clouds.

I. INTRODUCTION

The research fields of Bose-Einstein condensation¹ (BEC) in dilute atomic gases and cavity quantum electrodynamics² (QED) with single atoms both push forward the understanding, engineering, and harnessing of quantum mechanical states. A Bose-Einstein condensate is a collective quantum state of a large atom sample and provides maximum control over external degrees of freedom. Optical cavity QED in the strong coupling regime allows probing and manipulation of single atoms with the quantized electromagnetic field in the cavity mode.

A Bose-Einstein condensate is a fascinating demonstration of the quantum character of matter where indistinguishable, weakly interacting particles populate the motional ground state and establish a macroscopic wave function. Its experimental realization^{3,4} in 1995 sparked an ongoing vivid experimental and theoretical research on this novel quantum state. Initial experiments highlighted its phase coherence,⁵ superfluidity^{6,7} and demonstrated the production of atom lasers.^{8,9,10,11} Current investigations explore quantum phase transitions,^{12,13} tunable atomic interactions,^{14,15} and particle correlations.^{16,17,18}

Similarly, the way to cavity QED in the optical domain was paved by first experiments in the 1990’s reaching the strong coupling regime and demonstrating vacuum Rabi splitting of the coupled atom-cavity system.¹⁹ In the strong coupling regime of cavity QED the atom field interaction dominates over the dissipative losses of the quantum system. An ultrahigh finesse cavity was used to demonstrate single atom detection in an atomic beam.²⁰ Recent experimental progress was made in the observation of the motional dynamics^{21,22} as well as the trapping^{23,24} and cooling^{25,26} of single atoms within the

cavity mode. This provides an avenue towards implementation of technologies and concepts for quantum information processing, such as nonclassical light sources^{27,28} and quantum state transfer.²⁹

The experimental combination of quantum degenerate gases with an ultrahigh finesse optical cavity offers fas-

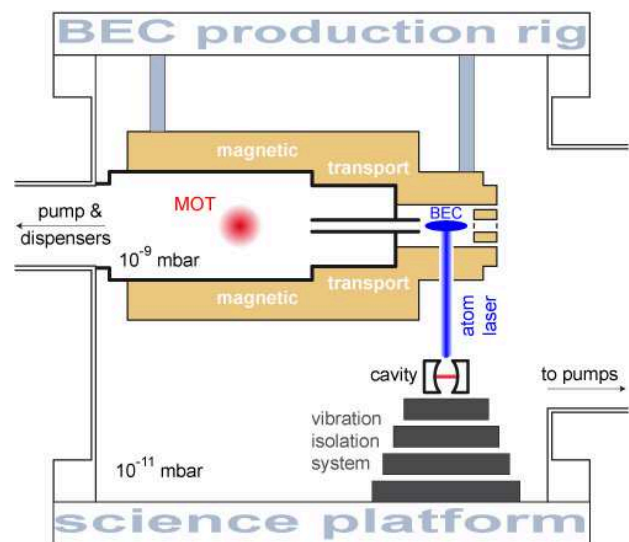


Figure 1: Schematic sketch of the experimental setup illustrating the nested vacuum chambers, the short magnetic transport and the “science platform” bearing the ultrahigh finesse optical cavity on top of the vibration isolation system. The atomic cloud captured in the magneto-optical trap (MOT) is transferred through a differential pumping tube into the ultrahigh vacuum region and evaporatively cooled towards quantum degeneracy. We output couple a continuous atom laser from the BEC and direct it to the cavity mode where single atoms are detected.

inating prospects^{30,31,32} for quantum atom optics. The first experiments detecting single atoms from a coherent matter wave field with an ultrahigh finesse optical cavity have recently been performed.^{17,33} This progress develops the new field of quantum atom optics where both matter and light fields are quantized. Cavity QED detection of single atoms is possibly nondestructive on the atomic quantum state and could be used to perform atom interferometry with squeezed states and precision measurements at the Heisenberg limit.³⁴ In addition, the single atom detection method offers an unprecedented sensitive and weakly invasive probe to investigate physical processes in ultra cold atomic clouds *in situ* and time resolved. On the other hand, Bose-Einstein condensates and atom lasers provide dense and coherent atomic sources with precisely controlled atomic external degrees of freedom for exploring and exploiting cavity mediated single atom single photon interactions.

The integration of an ultrahigh finesse optical cavity in a Bose-Einstein condensation system, despite being a central goal for atom chips,^{35,36} has only recently been achieved^{17,33} with the apparatus described here. The experimental difficulties in merging these two experimental research fields arise mainly from adverse vacuum requisites and sophisticated topological requirements on both of these state-of-the art technologies. For example, limited spatial access prevents the inclusion of a high finesse optical cavity in conventional Bose-Einstein condensation setups.

Our apparatus (Fig.1) overcomes the experimental challenges of integrating an ultrahigh finesse optical cavity into a Bose-Einstein condensation machine with a conceptually novel design. It provides spacious access to the condensate for divers samples and probes which are modularly integrable on our science platform. This is rendered feasible by means of a nested vacuum chamber design, a high vacuum (HV) enclosure inside the ultrahigh vacuum (UHV) main chamber and a short *in vacuo* magnetic transport. Two distinct pressure regions are required since the two common stages towards Bose-Einstein condensation, a magneto-optical trap (MOT) for laser cooling and trapping a large number of atoms and evaporative cooling, have conflicting requirements on their vacuum environment. We utilize a short magnetic transport^{37,38} to convey the cloud of cold ⁸⁷Rb atoms from the MOT to the main chamber, where we perform evaporative cooling to quantum degeneracy. From the Bose-Einstein condensate we output couple a continuous atom laser and direct it into the cavity mode. The ultrahigh finesse optical cavity is integrated on the so-called science platform and rests on top of an UHV compatible vibration isolation system which is vital for its stable operation. The cavity is located 36 mm below the BEC and enables us to detect single atoms from a quantum degenerate source.

In the following, the modular experimental building blocks of our hybrid BEC and cavity QED apparatus are presented in more detail. Then we de-

scribe the operation and highlight the performance of our quantum atom optics experiment.

II. VACUUM SYSTEM: THE NESTED CHAMBERS CONCEPT

The vacuum system presented here consists of two nested steel chambers where the higher pressure (HV) MOT chamber is situated inside the lower pressure (UHV) main tank. The HV region houses the alkali dispenser source. Both vacuum regions are pumped separately and a differential pumping tube maintains a pressure ratio of 10^2 . The setup grants multiple optical access for laser cooling as well as for observation and manipulation of the resulting Bose-Einstein condensate.

A. Main chamber

The objective of the vacuum system (Fig.2) is to attain an UHV environment at 10^{-11} mbar for efficient evaporative cooling of the laser precooled atomic cloud. Centerpiece of our vacuum system is the custom-welded, cylindrical main tank of nonmagnetic stainless steel (AISI type 316).⁴² It has a diameter of 20 cm and features multiple access (see Fig.3) in form of optical grade viewports and electrical feedthroughs with standard CF sealing. The viewports are antireflection coated on both sides.

Two custom-made CF 200 cluster flanges cap the main chamber from above and below. The top flange (called “BEC production rig”) features optical and electrical access (Fig.3) since most of the electromagnetic coil configuration is mounted on this flange and placed inside the UHV. In addition a liquid nitrogen compatible feedthrough is supplied for cooling the magnet coils and resistive temperature sensors (PT100) are used to monitor their temperature. The bottom flange (called science platform) serves as an exchangeable mount for the inclusion of samples and probes into our system. Besides viewports and electrical feedthroughs (Fig.3) to connect to electromagnetic coils, PT100 sensors and the piezo element of the optical cavity design, it includes a cold finger and a 3001/s nonevaporable getter (NEG) vacuum pump.

The core vacuum pumping is performed by a titanium sublimation pump and a 1501/s ion getter pump. A right angle valve is included in this pumping section for rough pumping the system.

The HV part of the system (Fig.2) connects to the MOT chamber which protrudes into the UHV main chamber and serves as a repository for rubidium atoms. It can be shut off with a gate valve between the MOT chamber and the rubidium dispenser source.^{39,40} The HV region is pumped by an ion getter pump (751/s) whose pumping speed can be derated by a rotatable disk inside the tube reducing its conductance. This serves to control the rubidium vapor pressure which is monitored with a

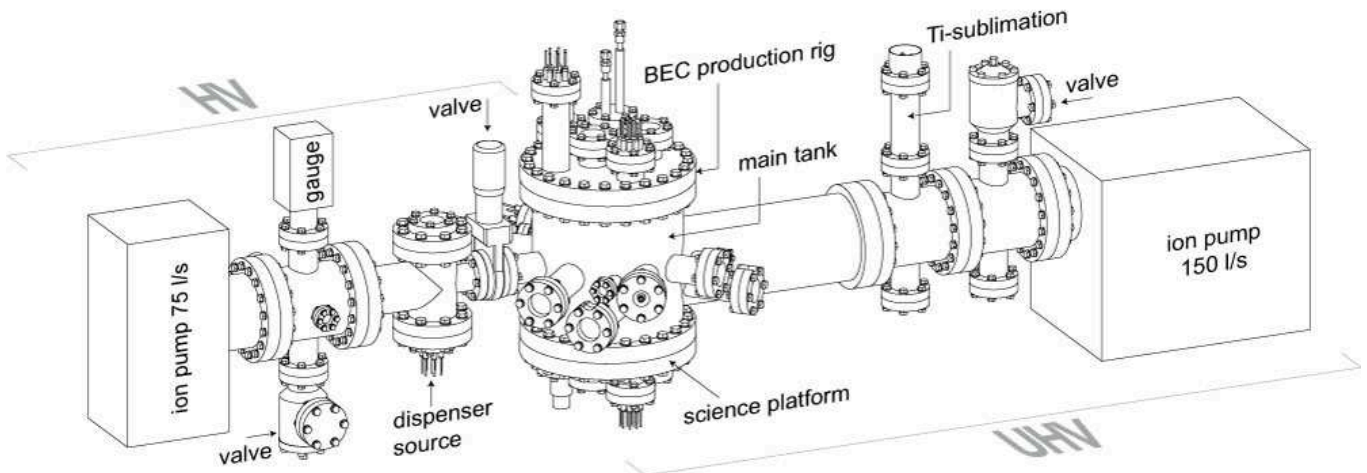


Figure 2: Overview of the complete vacuum system showing the pumping sections for the two nested vacuum regions, high vacuum (HV) and ultrahigh vacuum (UHV), respectively. The overall length is close to 2 m. The main tank offers multiple optical and electrical access and is sealed off by two CF 200 cluster flanges called “BEC production rig” and “science platform.”

wide range pressure gauge. Also a right angle valve is included for rough pumping purposes.

Our rubidium repository consists of seven alkali metal dispensers fixed in star shape to the tips of an eight pin molybdenum electrical feedthrough where the center pin serves as the common ground. Beforehand, the conductors were bent by 90° so that the dispensers aim towards the MOT chamber. Dispenser operation may be viewed through a viewport mounted from above. The dispensers can easily be exchanged without breaking the ultrahigh vacuum in the main chamber by closing the gate valve between the MOT chamber and the dispenser source.

B. MOT chamber

The MOT chamber as part of the high vacuum region is situated inside the ultrahigh vacuum main tank (Fig. 3). However the fact that both pressure regions are well in the molecular flow regime allows for relatively simple sealing techniques. The purpose of the MOT chamber is to contain a higher background vapor pressure of rubidium atoms for an efficient loading of the magneto-optical trap.

Our MOT chamber was milled out of a single block of nonmagnetic stainless steel (AISI type 316). This material was chosen to reduce eddy currents produced by fast switching of the magnetic fields. Bores of 35 mm diameter give optical access for the six pairwise counter-propagating laser beams forming the magneto-optical trap. These bores are sealed off by standard optical grade laser windows (BK 7) with double-sided antireflection coating and clamped to the MOT chamber by stainless steel brackets. At the metal glass interface we use thin (0.2 mm) Teflon rings to protect the windows. Additionally we took precautions in the form of ceramic

screens to prevent coating of the windows by the titanium sublimation pump.

An additional bore provides the connection of the MOT chamber to the HV pumping section and the dispenser source. This connection is sealed against the UHV main tank with a tight fit stainless steel bushing inside the CF 40 socket. The bushing is tightened to the MOT chamber thereby pressing its circular knife edge into a custom-made annealed copper gasket. A screen to prevent a direct line of sight from the hot dispensers to the center of the MOT is included in the laser cut gasket.

The MOT chamber is sandwich mounted between the two magnet coil brackets for the magnetic transport (see Sec. III) and simultaneously functions as a spacer for the magnet coil assembly. The whole structure is suspended from the top flange by four M8 thread bars and represents our BEC production rig.

A differential pumping tube interfaces the MOT chamber with the main tank. It serves for conveying the cloud of cold atoms with the magnetic transport from the MOT into the UHV main chamber. The aluminum differential pumping tube is mounted with a press fit in the MOT chamber and can be exchanged. It has an inner diameter of 6 mm over a length of 45 mm and can maintain a differential pressure of 10^2 - 10^3 depending on the actual pumping speed in the UHV main chamber. Its conductance for rubidium at room temperature is about 0.31/s.

C. Installation

All components of the system were electropolished (the custom-welded parts were pickled afore), cleaned and air baked at 200°C before assembly.⁴¹ Additionally, all critical *in vacuo* materials like Stycast 2850 FT⁴³ and Kapton⁴⁴ used for the magnet coil brackets (see Sec. III),

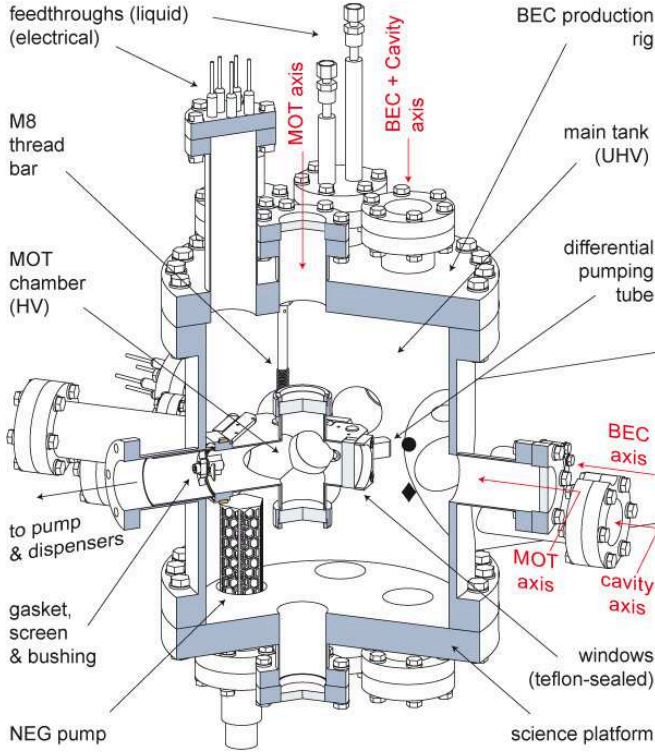


Figure 3: Section through the UHV system illustrating the realization of the nested chambers design and revealing the details and objectives of the diverse optical axes. The position of the BEC and cavity are marked by (•) and (♦), respectively. The high vacuum MOT chamber is suspended from the “BEC production rig” and sealed by a tight fit bushing against the UHV main tank. The “science platform” provides space for additional components such as the ultrahigh finesse optical cavity. [Note: For clarity in the illustration the magnet coil configuration (Fig. 5) and the optical cavity assembly (Fig. 8) are omitted in this figure.]

Viton A⁴⁵ and Wolfmet⁴⁶ utilized for the vibration isolation stack (see Sec. IV) as well as plastic (Teflon⁴⁷, Vespel⁴⁸) and ceramic (Macor⁴⁹, Shapal⁵⁰) parts were externally outgassed by vacuum baking them at 200 °C.

The bakeout⁵¹ of the fully assembled system was performed at 120 °C which is the maximum temperature rating of the piezotube used in our optical cavity assembly. The ultimate attainable pressure in the UHV system is 3×10^{-11} mbar. It is measured directly inside the main chamber in close proximity of the magnetic trap for Bose-Einstein condensation. In the HV part we maintain a pressure in the range of 10^{-9} mbar.

III. MAGNETIC FIELD CONFIGURATION: TRANSPORT, TRAP AND SHIELDING

A magnetic transport^{37,38} is a reliable and controlled way to transfer the cold atomic cloud from the MOT to a region of considerably lower background pressure for evaporative cooling. Only an *in vacuo* magnet coil

arrangement in conjunction with nested vacuum domains allows for a short transport design and grants spacious access volume inside the main chamber. However care must be taken to meet the UHV requirements with the materials chosen for the magnet coil structure.

Besides spatial and optical accessibilities the requirement on the magnetic trap is mainly magnetic field stability to enable stable atom laser output coupling. Therefore we employ a magnetic trap in the quadrupole Ioffe configuration⁵² (QUIC) because its simplicity allows for a compact design and ensures an easy and stable operation at very low power consumption (~ 2 W).

A magnetic shielding enclosure and additional *in vacuo* coils for manipulating atoms in connection with the cavity round off the magnetic configuration of the system.

A. Magnetic transport

The magnetic transport design consists of two partially overlapping electromagnetic coil pairs (called “MOT coils” and “transfer coils”) producing quadrupole potentials and the final QUIC trap coils [Fig. 4(a)]. The overall potential minimum can be moved over a distance of 82 mm so that the cold atoms in a low field seeking Zeeman state are conveyed from the position of the MOT directly into the final magnetic QUIC trap. The transfer coil pair provides sufficient overlap between the two

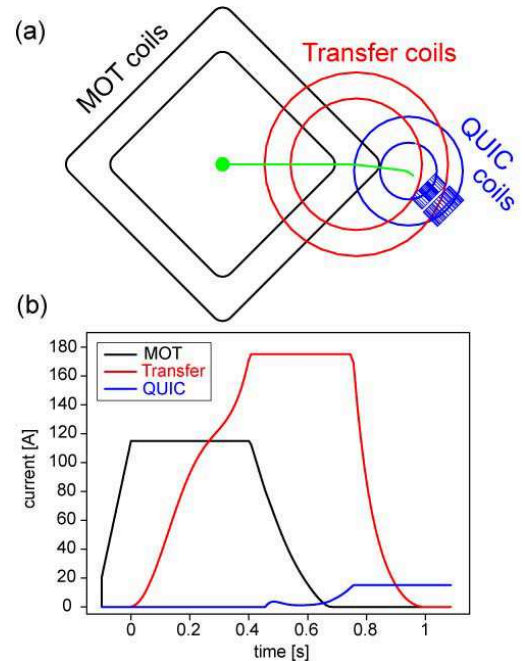


Figure 4: (a) Top view of the arrangement of coils for the magnetic transport. The line denotes the trajectory of the atomic cloud from the MOT (filled circle) into the QUIC trap. (b) Temporal sequence of currents through the different coils to realize the compression of the cold atomic cloud (negative times) and the magnetic transport.

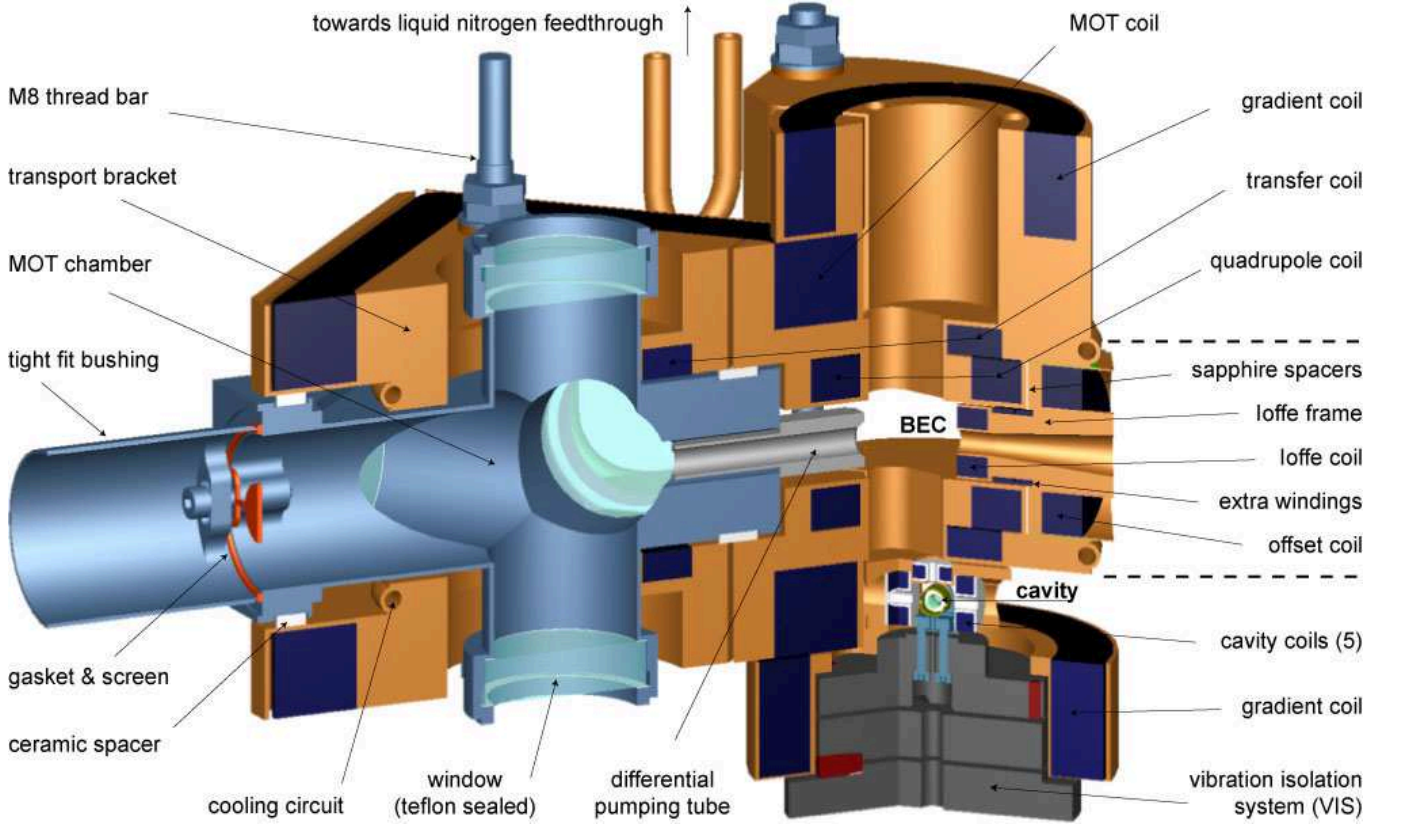


Figure 5: Section through the complete assembly inside the main vacuum chamber. It illustrates the arrangement of magnet coils, the inner chamber, and the cavity with respect to each other. Functional units of the magnet coil configuration are the two transport brackets that sandwich the inner chamber and the laterally mounted Ioffe frame (elements between dashed lines). These parts, including the top gradient coil, are fixed to each other and mounted from the top flange. The optical cavity on top of the vibration isolation system, the surrounding coils, and the bottom gradient coil are mounted on the science platform.

to achieve a smooth transfer of the magnetic potential without significant heating of the cold atomic cloud.

The magnet coils were wound from rectangular copper wire (3×1 and 1×1 mm) for optimal filling fraction. We choose Kapton film isolated wire which is temperature durable and suitable in the ultrahigh vacuum environment. The coils were integrated in two mirror-inverted, custom-made copper brackets and encapsulated with Stycast 2850 FT, a thermally conductive epoxy. The brackets are slotted in order to suppress eddy currents from switching the magnetic field. The magnet coil assembly was fixed in a sandwich structure around the MOT chamber and suspended from the top flange by M8 thread bars (Fig. 5). The complete assembly including the QUIC trap represents the BEC production rig.

A cooling system to remove the heat dissipated by the electromagnetic coils is supplied in form of a copper pipe with 4 mm inner diameter. It is soldered in a loop around each coil bracket and connected to the liquid nitrogen feedthrough. A temperature stabilized recirculating chiller⁵³ permanently pumps pure ethanol cooled to -90°C through the system. Thereby we maintain a maximum operating temperature below 0°C . This in turn lowers the power consumption. The surface tem-

perature of the coils is monitored with PT 100 sensors and interlocked to the power supplies.

The geometry and arrangement of the magnetic transport coils [Fig. 4(a)] are dominated mainly by constraints set by the size of the MOT chamber, the required length of the differential pumping tube, and the optical access to the MOT, BEC, and cavity. For instance, the square shape of the MOT coils best achieves a large overlap with the transfer coils while granting optical access to the cavity axis. However, the aspect ratio A/R of the coil separation ($2A$) to the coil radius (R) could be tuned to a balanced tradeoff between a maximally strong ($A/R = 0.5$) and a maximally long ($A/R = 0.87$) linear gradient region.⁵⁴ Anti-Helmholtz configuration is advantageous for tight confinement and deep trap depths whereas long linear gradients yield large handover regions between two coil pairs. Furthermore, the power consumption of a coil pair for a given field gradient can be minimized by choosing a well matched ratio of axial to radial windings.

In order to find an optimum current sequence for the magnetic transport³⁷ we calculate the magnetic field of the coil configuration analytically and discretize it along the transport axis on a $100\ \mu\text{m}$ grid. The currents needed to transfer the magnetic minimum smoothly from the

Table I: Electromagnetic properties of the magnet coils.

		MOT	Transfer	QUIC
Resistance	(m Ω)	200	50	300
Inductance	(μ H)	1000	70	450
Maximum current	(A)	115	170	15
Maximum field gradient	(G/cm)	310	290	320

MOT to the QUIC are then computed numerically in accordance with several constraints. Limited by a maximum available electrical current we optimized the magnetic field gradients and trap depths especially during the handover. Furthermore we tried to minimize deformations of the trapping potential. The resulting spatial sequence of currents per coil is converted into a temporal sequence including an acceleration and deceleration phase by taking into account the limited bandwidth of the current control servo [Fig. 4(b)].

The magnetic transport sequence initiates with a fast (400 μ s) ramp to 20 A in the MOT coils after magneto-optical trapping and optical pumping the cold atoms into a low field seeking state. The ramp needs to be fast with respect to the expansion of the cloud but adiabatic on the spin degree of freedom. It is followed by a slow (100 ms) compression of the atomic cloud to the maximum field gradients. Increasing the current in the transfer coils pulls the atoms towards their center and by decreasing the MOT coil current the zero of the potential is handed over [Fig. 4(b)]. The field of the QUIC is aiding at this point to maintain a constant aspect ratio. The magnetic transport finishes by ramping down the current through the transfer coils in favor of the QUIC coils. The atomic cloud is conveyed through the differential pumping tube directly into the magnetic QUIC trap which stays on for the subsequent evaporative cooling stage.

The trajectory of the magnetic transport [Fig. 4(a)] is slightly bent such that atoms in the final magnetic trap position have no direct line of sight into the higher pressure MOT chamber. This suppresses background gas collisions which would shorten the lifetime of the Bose-Einstein condensate. The bend is achieved by laterally offsetting the center of the QUIC trap by 3 mm from the differential pumping tube.

The MOT and transfer coils are powered by general purpose interface bus (GPIB) controllable 5 kW dc power supplies.⁵⁵ However, since their internal current control bandwidth is too slow to sample the time-current sequence for the MOT coils we externally feedback control it by a closed-loop servo. It is implemented with a current transducer and a MOSFET bench. The fast initial ramp to 20 A is additionally supported by current from four large capacitors (1 mF) charged to 60 V. The electromagnetic properties of the coils with resulting maximum currents and field gradients are listed in Table I.

The magnetic transport is performed over a period of 1 s. We maintain a minimum trap depth of ~ 70 G equivalent to about 2 mK. The total power required is approxi-

mately 2 kW which corresponds to an average power consumption of ~ 34 W at a duty cycle of 1/60.

B. QUIC trap

The magnetic QUIC trap consists of three coils connected in series. This is advantageous to diminish relative current fluctuations and therefore magnetic field fluctuations. Two coils (called “quadrupole coils”) produce a quadrupole field and one smaller coil (called “Ioffe coil”), mounted orthogonally between the quadrupole coils lifts the magnetic zero to a finite value and adds a curvature to the resulting potential.⁵² Having a nonzero magnetic minimum is crucial when evaporatively cooling atoms towards quantum degeneracy in order to circumvent losses due to Majorana spin flips.

The geometry of the QUIC trap potential is approximately cylindrically symmetric with respect to the Ioffe coil axis. Along this direction the curvature and therefore the confinement is weaker than in the radial directions. In our case this results in cigar shaped Bose-Einstein condensates with an aspect ratio of 5:1.

The exact position and dimension of the Ioffe coil are very critical to yield the desired magnetic bias field B_0 which should be on the order of a few Gauss. A low bias field is preferential because the trap frequencies scale as $B'/\sqrt{B_0}$, where B' is the magnetic field gradient and high trap frequencies permit faster and more efficient evaporative cooling.

The construction of the Ioffe coil is done in the same way as for the transport coils. It is integrated in a slotted copper frame and potted with Stycast. The Ioffe frame is mounted laterally between the transport coil brackets which hold the quadrupole coils. Additionally, the Ioffe frame serves as a spacer for the two transport brackets. The mechanical contact is accomplished with sapphire sheets in order to prevent eddy currents by simultaneously maintaining good thermal conductivity (Fig. 5). The large mass of the complete magnet coil structure functions as a thermal low pass filter which contributes to the good temperature stability.

In the Ioffe frame we have integrated additional coils on the same axis as the Ioffe coil to be able to manipulate the final trap geometry inside the vacuum system after bakeout. Two few-winding coils are employed to fine-tune the value of the magnetic field minimum B_0 . One larger coil (called “offset coil”) a little further away from the trap center can be used to change the aspect ratio of the trap and make it approximately spherical. Furthermore, the Ioffe frame features a conical bore which allows us to image the BEC through the center of the Ioffe coil.

The electrical connections of the coils forming the magnetic QUIC trap are realized outside the vacuum. We have included a 1.4 MHz low pass filter in parallel to the Ioffe coil to avoid any radio frequency (rf) pickup because of its low inductance of 4 μ H. The QUIC trap is operated with a 150 W power supply⁵⁶ specifically tuned to

our inductive load. The average power consumption of the magnetic trap is maximally 60 W but can be as low as 2 W when operated at 3 A (see Sec. V).

C. Magnetic shielding

We clad the main vacuum chamber in a mu-metal shielding (Fig. 6) to minimize the influence of residual external magnetic field fluctuations on the cold atoms. A magnetically quiet environment is essential for stable continuous wave (cw) operation of the atom laser.

Mu-metal is a magnetically soft nickel alloy with a very high magnetic permeability $\mu \sim 10^5$ which attenuates magnetic fields inside a cohesive enclosure. The screening effect depends very much on the completeness of the mu-metal box. Magnetic field lines penetrate an opening roughly as far as its diameter. Therefore we have attached a stub around the pumping tube of the main vacuum tank to attain a better aspect ratio at the position of the BEC. The design of the mu-metal hull was aided by computer simulations of the electromagnetic field. The mu-metal was machined and cured as recommended by the manufacturer.¹⁰⁰ After demagnetization we have measured a dc magnetic extinction ratio of ~ 40 in the vertical and ~ 100 in the horizontal direction at the position of the BEC.



Figure 6: Photograph of the preassembled mu-metal hull before it is mounted around the main vacuum tank. It consists of seven large and several small individual pieces.

D. Auxiliary coils

Since the mu-metal shielding prevents any manipulation of the atoms with external magnetic fields, we

have arranged supplementary magnet coils inside the mu-metal enclosure. All extra coils were potted with Stycast either in a slotted copper or Shapal frame for good thermal conductivity and mechanical sturdiness.

Two large coils (called “gradient coils”) are included in the main vacuum chamber to compensate the gravitational force for the weakest magnetic sublevel (30.5 G/cm) with 22 A. Their total resistance and inductance is about 0.2Ω and 0.9 mH, respectively. The gradient coils were mounted inside the vacuum chamber on the transport bracket (Fig. 5) and on the science platform around the cavity (Fig. 8), respectively. With the latter we should be able to reach the widest Feshbach resonance of ^{87}Rb ($\sim 1008 \text{ G}$)⁵⁸ at the position of the cavity.

Around the cavity we have placed two pairs of tiny coils (4Ω , 0.4 mH) along and perpendicular to the cavity axis (Fig. 5). They can be used to create magnetic field gradients of about 200 G/cm (with 1 A) for tomography experiments. In combination with a fifth tiny coil (1Ω , 0.1 mH) mounted above a magnetic trap at the position of the cavity can be formed. These five small coils (called “cavity coils”) were wound from 0.04 mm^2 Kapton isolated copper wire on Shapal frames to be penetrable by radio frequency.

In addition to the magnet coils inside the vacuum tank we have wound three mutually orthogonal pairs of large extra coils around the main tank. However, they are still within the mu-metal hull and serve to produce homogeneous magnetic fields, e.g., for optical pumping.

IV. SCIENCE PLATFORM: IMPLEMENTATION OF THE OPTICAL CAVITY

We have designed this apparatus with attention to versatile access for samples and probes to the BEC. Therefore we have implemented two independent sections of complementary functionality, i.e., the BEC production rig (see Secs. II and III) and the science platform. The latter is a modular, interchangeable flange, which in the current configuration supports our single atom detector in form of the ultrahigh finesse optical cavity.

The design of the cavity was guided by the need for stability, compactness, and ultrahigh vacuum compatibility. It rests on top of a passive vibration isolation stack which can be positioned on the science platform.

A. Cavity design

The Fabry-Pérot optical cavity is formed by two dielectric Bragg mirrors of ultrahigh reflectivity and ultralow scattering losses.⁵⁹ The reflection band is 40 nm wide and centered around 780 nm. We have determined an ultimate quality factor $Q = 1.6 \times 10^8$ after bake-out from the linewidth of the cavity ($\Delta\nu = 2.4 \text{ MHz}$). The initial Q immediately after cleaning the mirrors was

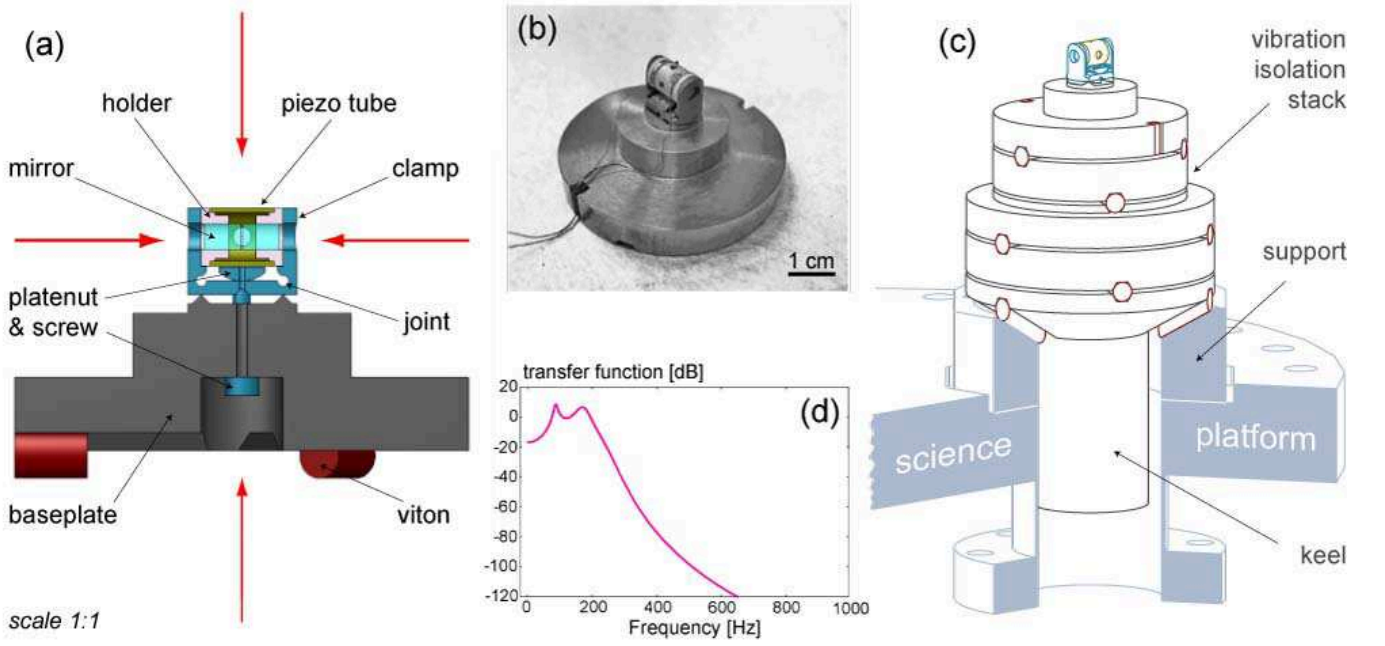


Figure 7: Elements of the optical cavity implementation. (a) Plane cut through the assembled cavity design where the arrows indicate optical access. (b) Photograph of the cavity setup. The electrical leads for the piezotube are pinched in a slotted Viton piece to efficiently decouple the cavity from the environment. (c) The cavity assembly resting on top of the vibration isolation stack which is positioned on the science platform. (d) Modeled frequency response of our vibration isolation stack.

higher by about a factor of two. The cylindrical mirrors (3 mm diameter, 4 mm length) having a radius of curvature of 77.5 mm are separated by $178 \mu\text{m}$ which results in a Gaussian mode waist of $w_0 = 25.5 \mu\text{m}$. We precisely measured the length of the near planar cavity by simultaneously transmitting two different known wavelengths (see Sec. V C) and determined a free spectral range of $\nu_{\text{FSR}} = 0.84 \text{ THz}$ from which we derive a finesse of $\mathcal{F} = 3.5 \times 10^5$.

Each mirror was bonded with superglue into a specifically fabricated ceramic (Shapal) ring structure. It positions and fixes the mirror inside the piezoceramic tube.⁶⁰ A piezo is required to fine-tune the length of the cavity ($\sim 0.5 \text{ V/nm}$) and as the actuator for the cavity lock (see Sec. V C). The 7 mm long piezotube⁶¹ has inner and outer diameters of 5.35 and 6.35 mm, respectively. It is equipped with nonmagnetic wraparound electrodes (silver) which allows the inner electrode to be contacted from the outside. Additionally, the piezotube features four radial holes of 1 mm diameter for lateral access of atoms and lasers perpendicular to the cavity axis.

The cavity assembly is mounted by a specifically designed compact fixture (called “clamp”) making use of mechanical joints [Fig. 7(a)]. It was manufactured by spark erosion from titanium in order to be nonmagnetic while having good elastic properties. Further design considerations aimed at high mechanical eigenfrequencies to avoid resonances within the bandwidth of the cavity lock ($\sim 40 \text{ kHz}$), that means a small size and high stiffness are favorable. We estimate the lowest eigenfrequency of

our fixture with a simple mechanical fixed-hinged beam model⁶² to be $\sim 50 \text{ kHz}$.

Our design of the cavity mount consists of the L-shaped clamp and a baseplate with integrated bearings to which the clamp is tightened with a plate nut. It converts the downward force onto the cavity assembly and firmly holds it together. Moreover it provides the piezo with a load. A hole of 1.2 mm diameter in the baseplate and plate nut grants optical access to the cavity from below. This cavity setup is highly modular and easily interchangeable because it freely rests on the vibration isolation stack [Fig. 7(b)].

B. Vibration isolation system

The aforementioned baseplate simultaneously acts as the top mass of our vibration isolation stack⁶³ which consists of five layers of massive plates (Wolfmet) with rubber dampers (Viton A) in between [Fig. 7(c)]. Viton has good vibration damping properties and is suitable for an ultrahigh vacuum environment. The 5 mm diameter Viton pieces rest in hexagonal grooves that are radially arranged in 120° graduations. Consecutive layers are rotated by 60° to prevent a direct “line of sound.” Hexagonal shaped grooves best avoid squeezing and creeping of the rubber and provide good lateral stability. Position, angle, and tilt reproducibility of this structure are excellent because of the frustum shaped bottom mass with keel. It centers the stack in an inverted, truncated cone-

like support and assures mechanical stability by lowering the center of mass below the support points. The complete stack has a central 10 mm bore for vertical optical access to the cavity.

Its damping properties can be modeled by regarding the structure as a system of coupled masses and springs⁶⁴ and calculating its frequency dependent transfer function [Fig. 7(d)]. For attenuation at low frequencies large masses and small spring constants are favorable.^{65,66} Therefore we have fabricated the plates from a heavy metal alloy (Wolfmet) and employed short (10 mm) Viton pieces. Our vibration isolation stack works well for acoustic frequencies above 200 Hz.

Additional precautions to counter low frequency excitations such as building vibrations include setting up the experiment on a damped rigid optical table in a basement laboratory having its own independent foundation and choosing a position with little floor vibration within this laboratory. The quality of the vibration isolation system is such that we could easily operate the cavity in the vicinity of a turbo-molecular pump. Furthermore the vibration isolation stack kept the cavity in place when the whole optical table accidentally dropped by about 2 cm as we tried to tilt it.

C. The science platform layout

The self-contained, interchangeable science platform flange was prepared to support and align the complete cavity mount. Its layout provides manual positioning ability of the cavity mount by ± 2 mm along and perpendicular to the cavity axis, respectively. This is rendered feasible by an octagonal support (nonmagnetic steel) of the vibration isolation stack which can be deterministically moved and fixed in a larger octagonal millout on the flange.

The second objective of the support is to erect the arrangement of cavity coils with the gradient coil (see Sec. III D) to be positioned around the cavity without direct contact. The coil assembly is mounted on two non-magnetic steel sustainers which are fixed to the vibration isolation support.

In order to remove the dissipated heat by the electromagnetic coils, we have connected the copper bracket of the gradient coil to a power feedthrough serving as a heat bridge, i.e., cold finger. Outside the vacuum the 19 mm diameter copper conductor can be connected to the cooling circuit and cooled to -90°C . The copper rod serves as the main drain for the heat because of the low thermal conductivity of the steel sustainers and support.

The mounting of the independent BEC production rig and science platform within the main vacuum chamber has to be noncontact but within a fraction of a millimeter. This results in a final position of the optical ultrahigh finesse cavity being 36.4 mm below the BEC. The orientation of the cavity axis is at 90° with the symmetry axis of the magnetic trap (Ioffe axis).

V. OPERATION: BEC, ATOM LASER, AND CAVITY

We operate the experiment periodically with a cycle time of 60 s. During each cycle we produce a new BEC from which we output couple an atom laser. It is directed to the ultrahigh finesse optical cavity situated 36.4 mm below the BEC where single atoms are detected. The cavity is probed by a resonant laser and its length is actively stabilized by an off-resonant laser with respect to the atomic transition.

The experimental sequence is fully computer controlled by a C++ program. Digital and analog channels interface the computer with the elements of the experimental setup.⁶⁷ The experiment is distributed on two self-contained optical tables, one for the laser system and one for the vacuum apparatus. They are linked by optical fibers.

A. BEC

We form a Bose-Einstein condensate of ^{87}Rb in dilute atomic vapor from a dispenser loaded magneto-optical trap by means of rf-induced evaporative cooling.^{38,68}

During the first 20 s of each cycle we load the magneto-optical trap with atoms from the pulsed alkali dispenser source.⁴⁰ The dispensers are operated at ~ 7 A with a temporal offset of -3 s to the actual MOT phase. We work on the D2 line of ^{87}Rb ($5^2\text{S}_{1/2} \rightarrow 5^2\text{P}_{3/2}$) at a wavelength $\lambda = 780$ nm. For the cooling transition on

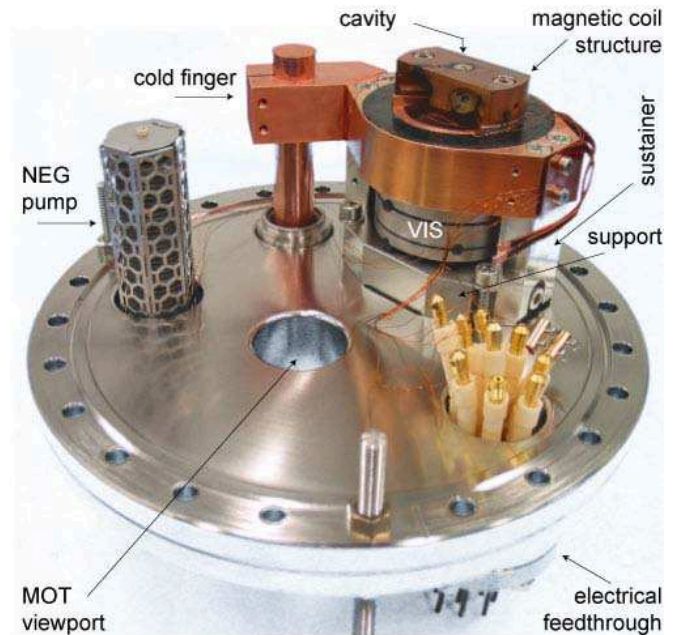


Figure 8: Photograph of the mounted science platform. The support bears the vibration isolation system (VIS) and the magnetic coil structure which surrounds the optical cavity.

the hyperfine ground state $|F=2\rangle \leftrightarrow |F'=3\rangle$ a laser power of 17 mW is employed in each of the six 34 mm diameter MOT beams. For optimum collection efficiency we choose a detuning of 3Γ , where $\Gamma = 2\pi 6$ MHz is the linewidth of the cooling transition. In order to be frequency tunable the laser is offset locked⁶⁹ from the $|F=2\rangle \rightarrow |F'=2\rangle$ transition by about 250 MHz and subsequently amplified with a tapered amplifier. An additional laser (called “repumper”) to avoid atomic losses into the $|F=1\rangle$ dark state is directly locked to the $|F=1\rangle \rightarrow |F'=2\rangle$ transition and delivers a power of 1 mW in each MOT beam. All our lasers are home built external cavity diode laser⁷⁰ locked by Doppler-free rf-spectroscopy technique⁷¹ to atomic transitions. For the magneto-optical trap we apply a magnetic field gradient of 10 G/cm by applying a current of 3.5 A to the MOT coils. Due to the mu-metal shielding no earth field compensation is required. We collect about 2×10^9 atoms with the magneto-optical trap before we switch off the magnetic field and sub-Doppler cool the atoms in a 10 ms optical molasses phase.

Before magnetically transporting the cold atomic cloud we optically pump the atoms into the low field seeking $|F=1, m_F=-1\rangle$ hyperfine state. Optical pumping is performed over 2 ms at a homogeneous magnetic field of 4 G. All light fields are off when the transport sequence starts with adiabatically compressing the cloud [Fig. 4(b)]. The magnetic transport conveys the atoms within 1 s through the differential pumping tube over a distance of 8 cm directly into the magnetic QUIC trap. We estimate a transport efficiency of $> 90\%$ by transferring the atoms back into the magneto-optical trap and measuring their fluorescence. The losses are mainly due to background collisions and depend on the pressure in the MOT chamber.

We operate the magnetic QUIC trap initially with a maximum current of 15 A. This yields the highest trap frequencies of $\omega_x = \omega_z = 2\pi 135$ Hz and $\omega_y = 2\pi 28$ Hz with a bias field B_0 of 4.7 G and a field gradient B' of ~ 300 G/cm. Here ω_y and ω_x denote the trapping frequencies along and perpendicular to the Ioffe axis, respectively and ω_z is in the vertical direction. Over a period of 23 s we perform rf-induced evaporative cooling with an exponential frequency ramp and a radio frequency power of 24 dBm. The radio frequency is radiated by a coil which consists of ten turns of Kapton clad copper wire (1 mm^2) encircling an area of 3 cm^2 . It is mounted 2 cm away from the center of the trap and is oriented at 90° with respect to the Ioffe axis. This results in a B_{rf} of about 30 mG at the position of the cold atoms.

Before reaching the critical phase space density for Bose-Einstein condensation we relax the trap to the final parameters of $\omega_x = 2\pi 38.5$ Hz, $\omega_y = 2\pi 7.3$ Hz and $\omega_z = 2\pi 29.1$ Hz with $B_0 = 1.2$ G and $B' = 60$ G/cm by powering the QUIC trap with 3 A. The initial trap symmetry is lifted by the large gravitational sag of about $290 \mu\text{m}$. It is given by $z_{\text{sag}} = -g/\omega_z^2$ where g is Earth's gravitational acceleration. Furthermore, the long axis

of the BEC is inclined by about 20° with respect to the horizontal plane. The opening of the trap is performed adiabatically ($\dot{\omega}/\omega \ll \omega$) over a period of 1 s. During this time a rf shield limits the trap depth to prevent heating of the cold atomic cloud. In the weak trap we further cool the atoms evaporatively over 5 s and achieve Bose-Einstein condensates of up to 5×10^6 atoms. The density in the weak trap is considerably lower so the losses due to inelastic collisions are reduced. We have measured a 1/e-lifetime for condensates of about 30 s. The typical size of the Bose-Einstein condensate is $12 \times 15 \times 60 \mu\text{m}^3$ (Thomas-Fermi radii) with a chemical potential μ of about 1 kHz.

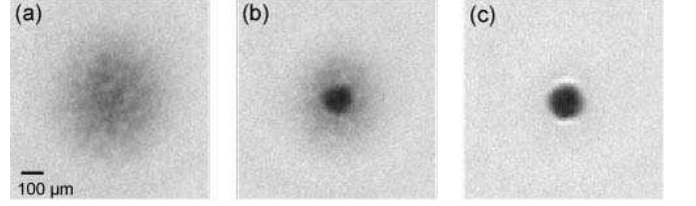


Figure 9: Absorption images of cold atom clouds. (a) Thermal cloud at a temperature T above the critical temperature T_c . (b) Bimodal distribution for $T < T_c$. (c) “Pure” Bose-Einstein condensate at $T \ll T_c$. The images were taken after 30 ms time of flight with a detuning of 2Γ to avoid saturation.

Resonant absorption imaging of the cold atoms after a free expansion time of 30 ms allows us to extract the number of atoms in the cloud and its temperature. We fit the resulting density distribution with the sum of a Gaussian and a Thomas-Fermi profile. The spatial resolution of our imaging system ($f/10$) is limited to $9 \mu\text{m}$ by the diameter of the windows. We employ a charge coupled device (CCD) camera with an according pixel size.⁷²

B. Atom laser

An atom laser is a coherent atomic beam extracted from a Bose-Einstein condensate (Fig. 10). The trapped condensate, being in a quantum degenerate state, serves as the source for the freely propagating atom laser. A steady-state output coupling process establishes a coupling between the ground state of the trap and the energy eigenfunctions of the linear gravitational potential and produces a continuous atom laser. The resulting cw atom laser,¹¹ in contrast to optical lasers, consists of interacting massive particles propagating downwards in the gravitational field. But like an optical laser it is a matter wave in a coherent state as defined by Glauber in the quantum theory for optical lasers⁷³ and exhibits higher order coherence.¹⁷

In order to output couple atoms we locally change their internal spin state from the magnetically trapped $|F=1, m_F=-1\rangle$ into the untrapped $|F=2, m_F=0\rangle$

hyperfine state. The spin flip is induced by a coherent microwave field at the hyperfine splitting frequency of ^{87}Rb ($\Delta E_{\text{hfs}}/\hbar = 6.8\text{ GHz}$).⁷⁴ This microwave output coupling scheme is equivalent to a two-level system because of the Zeeman splitting in the hyperfine niveaus ($\sim 1\text{ MHz}$). Therefore it is superior to rf output coupling which mutually couples all states from a Zeeman manifold.⁷⁵ The microwave signal is produced by a global positioning system (GPS) disciplined synthesizer.⁷⁶ We use a home-built resonant helix antenna with 14 dB gain [Fig. 10(a)] placed inside the ultrahigh vacuum chamber to radiate the microwave field. The antenna is connected and impedance matched to a commercial microwave feedthrough.

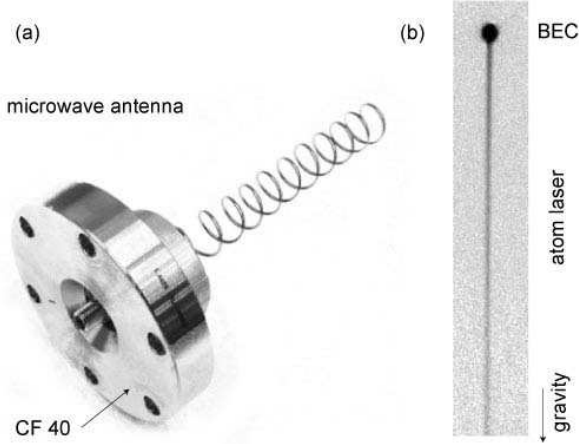


Figure 10: Coherent microwave output coupling of a continuous atom laser. (a) Helix antenna built for 6.8 GHz mounted on a vacuum feedthrough. (b) Resonant absorption image of the atom laser after a propagation of 2 mm.

The energy conservation for the microwave output coupling resonance condition is only satisfied at regions of constant magnetic field where $\Delta E_{\text{hfs}} - g_F m_F \mu_B B(\mathbf{r}) = \hbar \nu_{\text{mw}}$. Here ν_{mw} is the microwave frequency, $B(\mathbf{r})$ the magnetic field of the trap at position \mathbf{r} , and μ_B the Bohr magneton. The hyperfine Landé g factor g_F and the magnetic spin quantum number m_F apply to the BEC state. The magnetic moment of the output coupled atoms is zero to first order.

The resonant regions for output coupling are ellipsoidal shells with the geometry of the magnetic trap, centered at the minimum of the magnetic potential. However, the center of the actual harmonic trapping potential for massive particles is lowered by the gravitational sag with respect to the magnetic field minimum. For our experimental conditions the gravitational sag is $\sim 290\text{ }\mu\text{m}$ and therefore the resonant output coupling shells intersect the Bose-Einstein condensate almost as horizontal planes.

The Rabi frequency Ω of the microwave output coupling process is given by $\mu_{12} B_{\text{mw}}/\hbar$, where μ_{12} is the magnetic dipole matrix element between the two coupled states and B_{mw} the magnetic field of the microwave radiation.⁷⁷ The magnetic dipole transition has selection rules $\Delta m_F = \pm 1$. In the weak output coupling regime

($\Omega \ll \omega_z$) an atom leaves the condensate much faster than the Rabi frequency and does not undergo Rabi oscillations.⁷⁸ The atom laser output coupling rate depends on the number of atoms in the condensate N_{BEC} and the overlap $|\langle \Psi_{\text{BEC}} | \Phi_E \rangle|^2$ between the BEC wave function Ψ_{BEC} and the energy eigenfunction Φ_E of the free atom laser^{79,80}. For given atom number N_{BEC} and microwave frequency the output coupling rate is proportional to Ω^2 and therefore to the power of the incident microwave radiation⁸¹.

Producing a coherent cw atom laser crucially depends on the temporal stability of the resonance condition. We take experimental care to avoid any fluctuations or drifts of the magnetic resonance position. A temperature controlled cooling circuit for the large mass magnet coil structure and a GPS locked synthesizer permit excellently reproducible conditions. The magnetic shielding enclosure together with the hermetic steel vacuum chamber eliminate external electromagnetic field fluctuations (see Secs. II A and III C). The only detectable noise source is the low noise current supply powering the magnetic QUIC trap. We have measured a magnetic field stability of better than $5\text{ }\mu\text{G}/\sqrt{\text{Hz}}$ (at 3 kHz) or $50\text{ }\mu\text{G}$ overall (bandwidth: 50 kHz), respectively. This enables us to produce second order coherent atom lasers and output couple a cw atom laser over the duration of the BEC lifetime. Due to the extremely low atom fluxes measurable with the cavity detector we do not have to deplete the condensate significantly.

The atom laser freely propagates downwards for 86.1 ms before entering the ultrahigh finesse optical cavity where single atoms are detected. The cavity is placed 36.4 mm below the BEC which results in a velocity of 0.84 m/s for the atoms traversing the cavity mode. This velocity corresponds to a de Broglie wavelength of about 5 nm which could be useful for applications in coherent atom lithography⁸² or as an atom laser microscope.^{83,84}

C. Cavity lock

In order to engage the ultrahigh finesse optical cavity as a single atom detector we have to stabilize its length to better than $0.5 \lambda/\mathcal{F} \approx 1\text{ pm}$ with respect to the wavelength of the probe laser.

We choose a cavity locking scheme⁸⁵ that allows us to independently adjust the frequencies of the cavity resonance (ω_c) and of the probe laser (ω_1). Furthermore it enables us to keep the cavity permanently locked even during atom detection since the action of a single atom transit on the far-detuned stabilization laser is negligible and vice versa.

The cavity lock is realized with a far-detuned master laser at 830 nm and a resonant master laser at 780 nm referenced to a ^{87}Rb line. They are frequency stabilized by means of Pound-Drever-Hall locks⁸⁶ to a transfer cavity having a free spectral range ν_{FSR} of 1 GHz. In order to be freely tunable the actual probe and stabi-

lization slave lasers are phase locked⁸⁷ with a frequency offset of 0-500 MHz to their respective master lasers. The length of the science cavity is then actively controlled by a Pound-Drever-Hall lock on the stabilization slave laser with a bandwidth of 38 kHz. We create the necessary sidebands for the lock with a home-built electro-optical modulator.⁸⁸ It works at 362 MHz to have the sidebands well off resonant with the cavity because its finesse \mathcal{F} for 830 nm is only 3.8×10^4 and therefore its linewidth 22 MHz.

We actively control the incident powers of the stabilization and probe laser on the cavity to about 2 μ W and 3 pW, respectively. In order to have a good spatial overlap, the two lasers are guided through the same optical fiber. Their power ratio of 10^{-6} is realized with an optical color filter. We can couple about 25% of the incident probe laser power into the cavity TEM₀₀ mode being limited by the nonoptimal impedance matching.

The atomic resonance (ω_a) we employ for single atom detection is the cycling transition $|F=2\rangle \rightarrow |F'=3\rangle$ of the D2 line of ⁸⁷Rb. It yields a maximum atom field coupling rate $g_0 = d_{\text{iso}} |\mathbf{E}_{\text{max}}| = 2\pi 10.4$ MHz, where we have assumed an isotropic dipole matrix element⁷⁴ d_{iso} and a maximum single photon electric field strength $|\mathbf{E}_{\text{max}}| = \sqrt{4\hbar c / (\epsilon_0 \lambda w_0^2 l)}$ according to our mode volume with a beam waist $w_0 = 25.5 \mu\text{m}$ and a cavity length $l = 178 \mu\text{m}$.

The atom field coupling rate g_0 is large compared to the dissipation losses being the cavity field decay rate $\kappa = 2\pi \Delta\nu/2$ and the dipole decay rate $\gamma = \Gamma/2$ where $\Gamma = 2\pi 6.1$ MHz is the natural linewidth of the excited state. Furthermore the inverse atom transit time τ^{-1} is orders of magnitude smaller than the coupling rate which means the atom is always in a quasi steady state with the cavity field during the transit. The relevant parameters of our experiment are thus $(g_0, \gamma, \kappa, \tau^{-1}) = 2\pi (10.4, 3.0, 1.2, 3 \times 10^{-3})$ MHz, which brings us into the strong coupling regime of cavity QED defined by $g_0 \gg (\gamma, \kappa, \tau^{-1})$.

VI. SINGLE ATOM DETECTION

The single atom detection with an ultrahigh finesse optical cavity²⁰ can heuristically be viewed as the refractive index of a single atom being sufficient to significantly shift the cavity resonance. Consequently, the transmission of an initially resonant, weak probe laser is measurably reduced. In quantum mechanical terms the coupling of a single atom with the quantized electromagnetic field in the cavity mode dominates the dissipation losses (strong coupling regime) which means the level splitting of the Jaynes-Cummings model^{89,90} can be resolved. On the other hand, the quantum mechanical detection process on the longitudinally delocalized atom within the atom laser beam projects and localizes them inside the cavity mode.³³

We can efficiently study these cavity QED interactions

of single atoms having an atom laser as an unprecedented bright, controllable, reproducible, and well defined atom source. Here we present experimental results that characterize the performance of our combined BEC and ultrahigh finesse optical cavity system.

A. Analysis

In order to identify single atom transits we record the transmission of a resonant weak probe beam through the cavity with a single photon counting module⁹¹ (SPCM). A typical recording showing single atom transits is presented in Fig. 11.

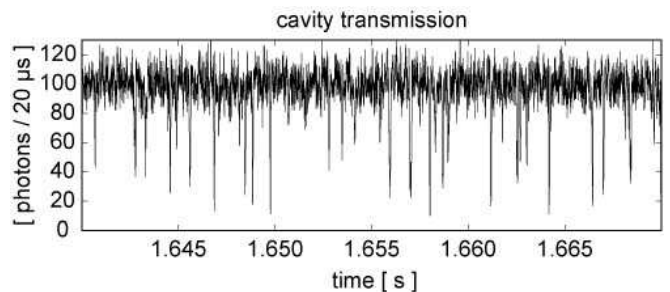


Figure 11: Cavity detection recording of an atom laser. The atom flux is about four orders of magnitude lower compared to Fig. 10(b). Single atom transits are clearly identified by their reduction of the shot noise limited empty cavity transmission.

The light coming from the cavity is filtered with a 780 nm band pass and a 830 nm notch filter to block the stabilization laser. Their combined relative optical density (OD) for 830 nm is 12. The SPCM is located inside a blackbox and exhibits an overall photon dark count rate of $\sim 100 \text{ s}^{-1}$.

The cumulative detection probability for intracavity probe photons taking into account losses in the optical system and the quantum efficiency of the SPCM is about 7%. It is mainly limited by the fact that we employ symmetric cavity mirrors with equal transmittivity (~ 2 ppm) and by the scattering losses (~ 7 ppm) of the mirrors.

In order to achieve a large signal-to-noise ratio for single atom detection we usually work with an average intracavity probe photon number of about 5.³³ This level corresponds to an intensity of about 40 times the saturation intensity and yields a photon count rate of $2\pi \Delta\nu \times 5 \times 7\% \approx 5 \text{ photons}/\mu\text{s}$.

We integrate the signal from the SPCM over 20 μs with a temporal resolution between 1-4 μs and set the criterion for single atom detection events to a reduction of more than four times the standard deviation (σ) of the shot noise limited empty cavity transmission. This reduces false atom detection events to less than 0.5 s^{-1} .

B. Characteristics of single atom events

The coupling of a single atom with the cavity mode can be characterized by the magnitude and duration of the resulting transmission dips. A recorded typical single atom transit is shown in Fig. 12(a). The 4σ threshold here corresponds to about 50% reduction in the probe light transmission of about 70 photons/ μs . We analyze detected events and show histograms in Figs. 12(b) and 12(c) for atom laser data taken in 184 iterations of the experiment. The atom flux was set to $\sim 1 \times 10^3 \text{ s}^{-1}$ so the probability¹⁷ for unresolved multiatom events within the dead time of our detector ($\sim 70 \mu\text{s}$) is less than 0.3%.

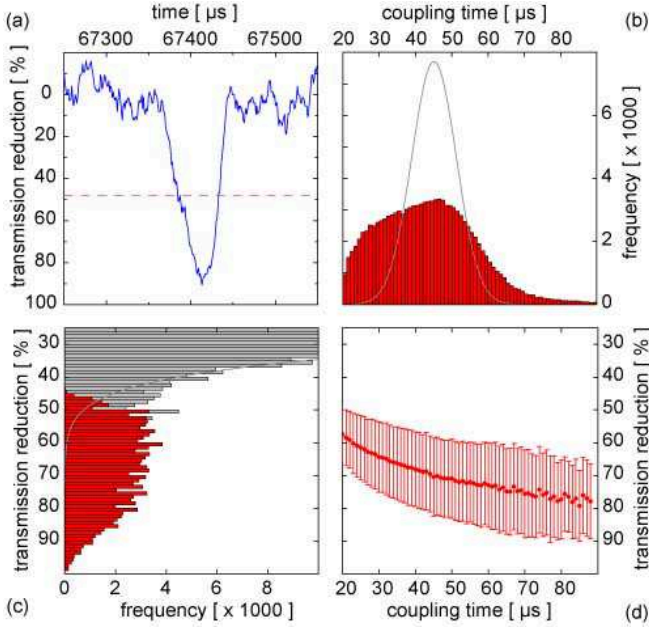


Figure 12: Characteristics of detected single atom events. (a) The transit of a single atom significantly reduces the probe light transmission through the cavity. We integrate the signal with a $20 \mu\text{s}$ sliding average and set the detection threshold to 4σ of the photon shot noise. (b) Distribution of measured coupling times (FWHM) [red] compared to the distribution of simulated events (gray). (c) Distribution of measured transmission reduction magnitudes. An evaluation with a 4σ threshold (red) is compared to a 2σ threshold [gray] revealing the discrimination of the events from the photon shot noise. (d) Dependency of the transmission reduction on the coupling time due to the non-Gaussian shape of the dips.

The dead time of our detector is reflected in the distribution of coupling times, i.e., the full width half maximum (FWHM) of the transmission dips [Fig. 12(b)]. It is mainly determined by the radial size of the Gaussian cavity mode and the velocity of the atoms during their transit. For a radial coupling strength $g(r) = g_0 e^{-r^2/w_0^2}$ with $w_0 = 25.5 \mu\text{m}$ and an initial velocity of 84.1 cm/s we expect an average coupling time of $45 \pm 12 \mu\text{s}$ [Fig. 12(b), gray]. Taking the classical free fall velocity is justified since the induced momentum uncertainty by projecting

the longitudinally delocalized atom into the cavity mode is on the order of $10 \mu\text{m/s}$.

In the numerical simulation we take into account photon shot noise and the features of our peak detect routine, namely, the $20 \mu\text{s}$ sliding average. The effect of the dipole potential on the transit time is negligible because the slight gain in velocity ($< 2 \mu\text{s}$) is counteracted by an effectively stronger and therefore longer coupling [Fig. 12(d)]. The mean of the measured coupling time distribution [Fig. 12(b), red] is in accordance with the expected value. However, the distribution deviates from the expected shape and exhibits an excess of short and long transit times. We attribute the shorter transits to optical pumping of atoms into the dark state $|F=1\rangle$ because their number is intensity dependent on the probe light. Longer transit times could be explained by diffraction of the atomic beam, scattering of spontaneous photons or cavity cooling effects, if the cavity axis is slightly nonorthogonal with respect to the atom laser (possibly 10^{-2} rad) and by unresolved multiatom events.

The magnitudes of the cavity transmission dips [Fig. 12(c)] reflect the different maximum coupling strengths for single atom transits. Depending on its radial position an atom will experience a varying peak coupling strength according to the Gaussian profile of the cavity mode. In the axial direction, however, the light force is strong enough to channel the atoms towards the intensity maxima of the standing wave.⁹² Arbitrarily weak coupling transits cannot be resolved due to the shot noise in the empty cavity transmission. We set the single atom detection threshold to 4σ of the original transmission to achieve a large signal-to-noise ratio.

The resulting histogram of peak depths is displayed in Fig. 12(c)(red) compared to data for a lower threshold level of 2σ in Fig. 12(c)(gray) unveiling the photon shot noise. The weakest detectable single atom events correspond to peak atom field coupling strengths of $g_0^{\min} = 2\pi 6.5 \text{ MHz}$. The strongest attainable coupling strengths for our cavity are $g_0^{\max} = 2\pi 10.4 \text{ MHz}$, which would be equivalent to a reduction of 80% in the cavity transmission.³³ We do not observe a sharp cutoff in the histogram but rather an equal distribution of transmission reductions from 50-80% with smeared out edges due to the comparatively large photon shot noise at the minimum of the transmission dip. This is consistent with numerical simulations for single atom events.

The dependence of remaining probe light transmission through the coupled atom-cavity system is nonlinear with the atom field coupling strengths.³³ Therefore the shape of the transmission dips is not Gaussian as the cavity mode and we observe a dependency of the magnitude in transmission reduction on the coupling time and vice versa [Fig. 12(d)].

The knowledge about the signatures of single atom events could facilitate the discrimination of “true” single atom events from “false” shot noise events or unresolved multiatom events, but the broad distributions make it difficult to distinguish two weakly coupling atoms from

a strongly coupling one. However, the observed characteristics of the detected events are in good agreement with the theoretical predictions for single atom transits. Moreover, these characteristics remain valid even when reducing the atom flux to very few single atom events.

C. Detector qualities

Having a BEC and an atom laser as the source for atoms that couple with the cavity mode offers several advantages. For instance it provides well reproducible starting conditions and allows us to precisely control the flux of atoms over a wide range by varying the microwave output coupling power. The attainable atom flux is orders of magnitude larger than in experiments employing a magneto-optical trap as the cold atom source.

We have confirmed that our single atom detector functions as a linear detector on the atom flux over three orders of magnitude (Fig. 13). The measured atom count rate is proportional to the output coupling microwave power (see Sec. V B). Saturation occurs at a flux of about 5×10^3 atoms per second. At higher rates multiatom arrivals within the dead time of our detector become dominant and single atom events cannot be resolved anymore.

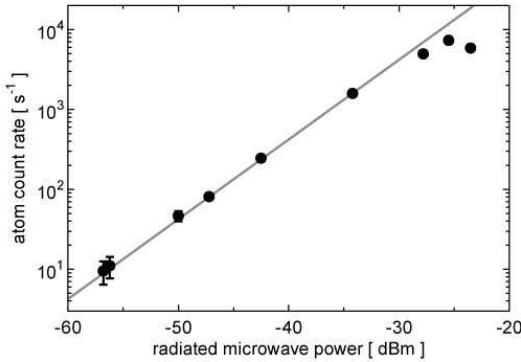


Figure 13: The ultrahigh finesse optical cavity functions as a linear detector on the output coupling rate, i.e., atom flux over three orders of magnitude. Saturation occurs at a count rate of about 5×10^3 atoms per second.

At a very low atom flux the error bars become increasingly large due to atom shot noise, i.e., the Poissonian distribution in the atom number determination. Additionally, a very weak atom “dark count” rate without intentional output coupling may be present. It is likely due to stray magnetic or optical fields and depends on the size of the Bose-Einstein condensate. However, the dark count rate is still less than 5 atoms per second on average for a BEC with 2×10^6 atoms, for instance.

D. Detection efficiency

The single atom detection efficiency of the ultrahigh finesse optical cavity strongly depends on the frequencies

chosen⁹⁴ for the probe laser (ω_l) and the cavity resonance (ω_c) with respect to the atomic transition (ω_a). Furthermore the effective coupling strength g_0 and therefore the detection probability are determined by the polarization of the probe light with respect to the quantization axis of the atomic spin.

In our experimental configuration we have a residual vertical magnetic field at the position of the cavity of about 16 G which represents the quantization axis for the atoms. The field originates from the magnetic QUIC trap which is on during the single atom detection in the atom laser.

We set the probe light to horizontal (within 10°) polarization which yields a four times higher atom count rate as vertically (within 10°) polarized light. Only these two distinct polarization settings are feasible since we experience a birefringence in the cavity resonance of about twice its linewidth. The horizontal polarization of the probe light produces a higher atom field coupling rate because it drives σ^+ and σ^- transitions compared to the fewer and weaker π transitions for vertically polarized light. The exact atom field interactions are more complex because of the Zeeman splitting and the resulting optical pumping dynamics inside the cavity.

However, for red detuned probe light the atoms entering the cavity in the $|F = 2, m_F = 0\rangle$ state will predominantly be pumped into the $|F = 2, m_F = -2\rangle$ stretched state and undergo cycling transitions driven by the σ^- polarization component. Therefore this cycling transition will be the main contribution in the single atom detection process. The imbalance is due to a redshift for the σ^- component and a blueshift for the σ^+ component of ~ 22 MHz in the magnetic field of 16 G at the cavity.

The number of detected atoms critically depends on the atom-probe laser detuning $\Delta_l = (\omega_a - \omega_l)/2\pi$ and probe laser-cavity detuning $\Delta_c = (\omega_l - \omega_c)/2\pi$ as illustrated in Fig. 14. Here ω_a refers to the bare atomic transition without magnetic field. For most efficient single atom detection we work with an atom - probe laser detuning $\Delta_l \approx 30$ -40 MHz and a probe laser - cavity detuning $\Delta_c \approx 0.5$ -1 MHz. By taking into account the 22 MHz Zeeman shift of the cycling transition $|F = 2, m_F = -2\rangle \leftrightarrow |F' = 3, m_{F'} = -3\rangle$ (vertical dashed line in Fig. 14) the probe laser red detuning for optimum single atom detection is about 3Γ . This value corresponds to the maximum of the dipole potential created by the probe laser, that means the dipole force channels the atoms in the axial direction towards the antinodes of the standing wave⁹² which are simultaneously the areas of the highest atom field coupling strength. In the radial direction the dipole force is too weak to significantly modify the trajectory of the atoms within the cavity mode. Also the dipole potential created by the stabilization laser is weak compared to the one created by the probe laser.

The second set of parameters in Fig. 14 where single atom transits are detected is around $\Delta_l \approx 18$ MHz and $\Delta_c \approx -1$ MHz. However, the count rate is reduced considerably because the probe light is blue detuned from

the cycling transition and therefore the dipole potential is repulsive. In the other two quadrants spanned by the resonances of the cavity and the cycling transition of Fig. 14 (dashed lines), atom transits result in increased probe laser transmission versus the empty cavity transmission.²⁴ We do not use those events for single atom detection because the efficiency is reduced by about a factor of 2 as compared to evaluating dips. Additionally the peaks exhibit a substructure consisting of single photon bursts which makes it more difficult to discriminate single consecutive atom transits.

In order to determine the detection efficiency for single atoms from the Bose-Einstein condensate we make use of the linear behavior of the atom flux on the microwave output coupling power (Fig. 13). We output couple a significant number of atoms measurable by absorption imaging while still in the weak output coupling regime. This number is compared to the number of atoms detected by the cavity with the corresponding factor of the output coupling powers.

We have calibrated the atom number in absorption imaging with the atom number at the critical temperature which is well known for our trap frequencies. For optimum settings of the cavity and laser detunings we are able to detect $(24 \pm 5)\%$ of the output coupled atoms with the cavity detector. This number is mainly limited by the spatial overlap of the atom laser beam with cavity mode (see Sec. VI E).

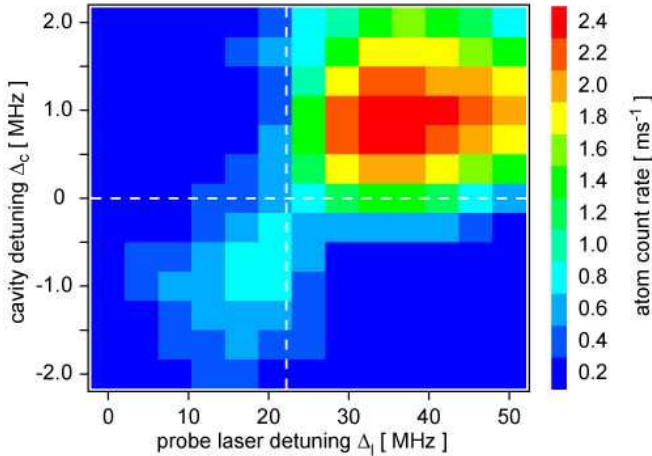


Figure 14: Dependence of the single atom detection efficiency on the probe laser Δ_l and cavity Δ_c detunings. The vertical dashed line represents the cycling transition which is Zeeman shifted by 22 MHz from the zero field atomic transition. Best single atom detection is performed with a probe laser red detuned by about 3Γ from the cycling transition and a cavity detuning of about $\Delta\nu/2$, corresponding to the maximum dipole potential created by the probe laser. The second local detection maximum corresponds to a blue detuned probe laser. Therefore the dipole potential is repulsive and the atom count rate reduced.

E. Alignment of the atom laser beam with the cavity mode

Obviously, in order to see single atoms with the cavity, the atom laser has to propagate through the cavity mode. However, this was not self-evident because the BEC production rig and the science platform are completely independent entities of the experimental apparatus and the alignment has to be better than a few millirad without knowing the exact position of the cavity mode. Furthermore, the second order Zeeman effect slightly bends the trajectory of the atom laser in the $|F=2, m_F=0\rangle$ state and modifies its final lateral position by hundreds of micrometers. Although we have aligned the cavity with respect to the BEC position as accurately as possible with plummets during the assembly of the apparatus, the atom laser did not innately hit the cavity mode. We correct these deviations by tilting the whole optical table on which the experiment rests employing its height adjustable legs. The tilt is monitored with a dual-axis inclinometer⁹³ having its axes aligned along and perpendicular to the cavity axis. With this method we aim the atom laser directly into the cavity mode [Fig. 15(a)] and maximize the atom count rate.

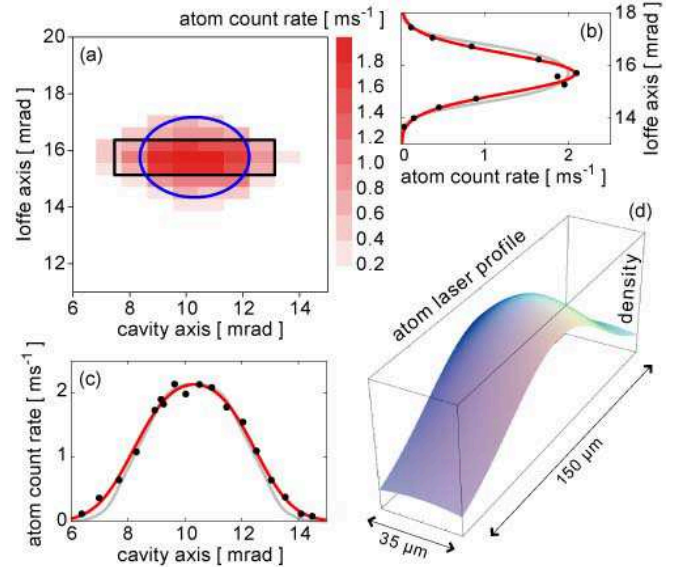


Figure 15: (a) The detected atom count rate for a constant atom flux is shown with respect to the inclination of the optical table along the two axes. The rectangle represents the active area of the cavity mode and the ellipse is the reconstructed size ($1/e$ diameter) of the atom laser at the position of the cavity. [(b) and (c)] Fit (red) to the measured data (black) by the convolution of the active size of the cavity mode with a Gaussian beam profile along the Ioffe (b) and cavity (c) axes. It is compared to the expected shape from numerical simulations of the Gross-Pitaevskii equation (gray). (d) Visualization of the extracted two-dimensional atom laser beam profile clipped by the active area of the cavity mode.

Moreover, tilting the experimental setup determinis-

tically enables us to deduce the diameter of the atom laser after a propagation of 36.4 mm. The active area of the cavity mode is approximately $35 \times 150 \mu\text{m}^2$. The size in the radial direction is determined by the weakest detectable atom transits corresponding to $g_0^{\text{min}} = 2\pi 6.5 \text{ MHz}$. In the axial direction it is given by the projection of the cavity length clipped by the curved mirrors.

A deconvolution of the measured angle dependent count rates with this active area, assuming a Gaussian atom laser beam profile, yields $1/e$ diameters of 80 and $110 \mu\text{m}$ along and perpendicular to the Ioffe axis, respectively [Figs. 15(b) and 15(c), red]. The mapped atom laser, being output coupled from the center of a Bose-Einstein condensate with 1×10^6 atoms, is slightly inverted compared to the trap geometry but almost round at the cavity. Here, its divergence along the fast axis, i.e., cavity axis, is about 2 mrad and less than 0.5 mrad along the Ioffe axis, which makes it the best collimated atom laser to date.^{10,11,95}

The repulsive mean field interaction from the remaining trapped BEC is considerable only along the fast axis where it acts as a defocusing lens for the atom laser beam. This results in an expansion about four times larger than expected from Heisenberg's uncertainty principle. Along the weakly confining Ioffe axis the lensing effect is negligible and the size of the atom laser is consistent with a free expansion of the initial ground state in the trap. The atom laser size and therefore its divergence, especially along the fast axis, can be further reduced by output coupling below the center plane of the BEC⁹⁵ and by smaller condensates (see Sec. VII B).

We compare the measured atom laser profiles along its symmetry axes with numerical simulations of the time evolution using the Gross-Pitaevskii equation. The resulting density distributions of the atom laser deviate slightly from a Gaussian shape,⁹⁶ but the measured convolutions with the cavity mode agree very well with the simulated curves [Figs. 15(b) and 15(c), gray]. The overestimated width along the Ioffe axis can be explained by the angle of the BEC axis with respect to the horizontal plane, reducing the spatial width of the output coupling region along the Ioffe axis.

Along the cavity axis the slight deviation at the edges is probably due to pointing variations, i.e., transverse oscillations of the atom laser beam. Small collective oscillations in the trap are translated into deflections of the atom laser beam over which we integrate with our detection method. The collective oscillations, mainly center of mass dipole oscillations in the trapped Bose-Einstein condensate, can be excited by radio frequency evaporation or incautious relaxation of the magnetic trap.

However, we can exploit this effect to precisely determine the frequencies of excited collective oscillations in the trap by analyzing the Fourier spectrum of the atom count rate. Such a spectrum is shown in Fig. 16 exhibiting harmonics of the trap frequencies (dipole oscillations) and mutual sidebands. The frequencies can be measured in situ with one and the same experimental implemen-

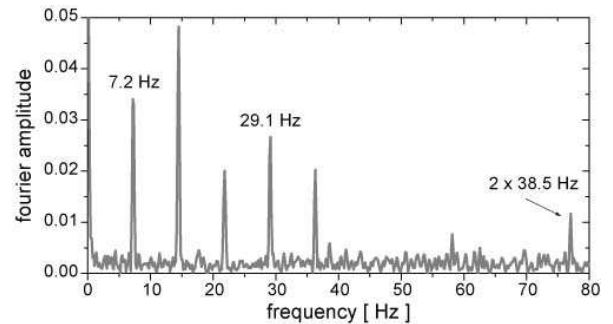


Figure 16: The Fourier spectrum of the detected atom laser flux exhibiting the trapping frequencies and their harmonics. A fast and precise tool to measure frequencies of collective oscillation in the trap.

tation of a Bose-Einstein condensate to high precision (mHz), Fourier limited by the duration of the atom laser recording.

F. Guiding the atom laser

The reason for the single atom detection efficiency not being unity is mainly the mismatch of the atom laser and cavity mode sizes [Fig. 15(d)]. Their overlap is only about 50% assuming a box given by the projected length of the cavity mode and a minimum peak atom field coupling strength of $g_0^{\text{min}} = 2\pi 6.5 \text{ MHz}$ in the radial direction. Calculating the atom trajectories taking into account the channeling effect of dipole potential we find a maximum single atom detection efficiency of 80% and an averaged efficiency of about 50% within this box. This is in good agreement that we detect about one quarter of the released atoms.

In order to increase the overlap and therefore the detectable number of atoms it is possible to funnel the atoms with a dipole potential created by a far red detuned guiding laser (850 nm, 15 mW, beam waists of $30 \times 60 \mu\text{m}^2$) into the cavity mode. By doing so we are able to improve the single atom detection efficiency by about a factor of 2 to around 50%. This number still differs from a perfect detection efficiency because the dipole potential formed by the probe laser is simply not strong enough to perfectly localize the atoms in the axial direction at the antinodes of the standing wave.

Although we are able to increase the single atom detection efficiency, employing the guiding laser involves some disadvantages. The scattering and heating rate in the dipole potential formed by the guiding laser can cause modifications of the atom arrival time statistics which is undesirable for many experiments.¹⁷ Furthermore, the guiding laser acts on both thermal and quantum degenerate atoms and therefore diminishes a characteristic feature of our detector, namely, the very sensitive discrimination of thermal and condensed atom count rates (see Sec. VII).

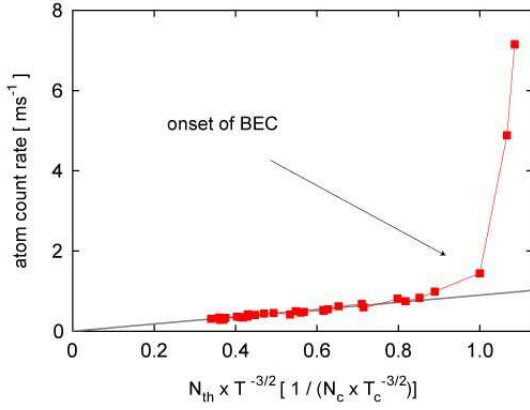


Figure 17: Investigation of atom count rates for thermal beams. The count rate is proportional to $N_{\text{th}} T^{-3/2}$ for temperatures above the critical temperature and sharply increases when cooling across the phase transition. Just above T_c the density and momentum distributions of the thermal cloud are governed by a Bose distribution and obey a different scaling law as expected for a Gaussian distribution.

VII. INVESTIGATION OF COLD ATOMIC GASES

The combination of a Bose-Einstein condensate with an ultrahigh finesse optical cavity enables us to detect single atoms from a quantum degenerate gas with very high sensitivity. Therefore we can employ the cavity as a minimally invasive probe for cold atomic clouds. This allows us to perform nondestructive measurements on the ensemble of cold atoms *in situ* and time resolved.

Assuming a constant weak output coupling power, the atom count rate of the cavity detector depends on the properties of the source via two factors. First of all the number of output coupled atoms is proportional to the number of atoms fulfilling the resonance condition, i.e., the one-dimensional density at the output coupling plane. And secondly the atom count rate depends on the probability for an output coupled atom to hit the cavity mode. Because of its finite active area the cavity functions as a filter in momentum space.

A. Thermal clouds

For a thermal cloud the density at the output coupling central plane is proportional to $N_{\text{th}} T^{-1/2}$ and the probability to hit the detector is proportional to $1/T$ assuming Gaussian density and momentum distributions. Therefore the thermal atom count rate detected with the cavity is proportional to $N_{\text{th}} T^{-3/2}$. This dependency is shown in Fig. 17. At the critical temperature of $T_c \approx 180$ nK for 10^7 atoms only about 0.6% of the output coupled thermal atoms will fly through the cavity mode and can possibly be detected.

The onset of Bose-Einstein condensation can be clearly

seen in the sharp increase in the number of detected atoms.^{97,98} Close to the critical temperature, however, the detected atom flux slightly deviates from the expected behavior because the approximated Gaussian distributions for density and momentum are not valid anymore near T_c . The thermal cloud is described by the more peaked Bose distribution which yields an increased atom detection rate of about 30% near the critical temperature of 180 nK compared to the Gaussian distribution.

B. Quantum degenerate gases

For Bose-Einstein condensates the probability for an atom to hit the cavity mode and therefore the atom count rate detected with the cavity is independent of temperature. The number of resonant atoms participating in the output coupling process is proportional to the density of the BEC and the area of the output coupling plane. This means the atom flux is proportional to $N_{\text{BEC}}^{4/5}$ because the Thomas-Fermi radius of a BEC scales as $N_{\text{BEC}}^{1/5}$.

However, this dependency is only true for Bose-Einstein condensates of intermediate size (Fig. 18) and deviates for very small and very large condensates. Output coupling from small condensates accounts for a faster quantum mechanical expansion of the initial ground state wave function in the atom laser. Therefore the overlap between the transverse atom laser wave function and the cavity mode is reduced. Large condensates on the other hand exhibit increased divergence because of the mean-field repulsion exerted on the atom laser propagating through the BEC. The condensate acts as an imperfect diverging lens and displaces the maximum density outward.^{95,96,99} This results in a weaker scaling of the detected atom flux with the number of atoms in the BEC and possibly a decrease when the atom laser profile becomes more “donut-mode-like.” These three regimes are displayed in Fig. 18 for measured atom count rates versus the number of atoms in the “pure” BEC. The exact position of the crossover between these regimes depends on the active area of the single atom detector.

C. Phase Transition

Our single atom detector in form of the ultrahigh finesse optical cavity is extremely sensitive and selective to quantum degenerate atoms not only because of the increased density at the output coupling region but also due to the filtering in transverse momentum space.

This means we can more accurately observe the onset of Bose-Einstein condensation as compared to absorption imaging techniques. The exact determination of the critical temperature, in combination with the precisely measured trap frequencies (Fig. 16), allows one in turn to calibrate the atom number obtained by the absorption images.

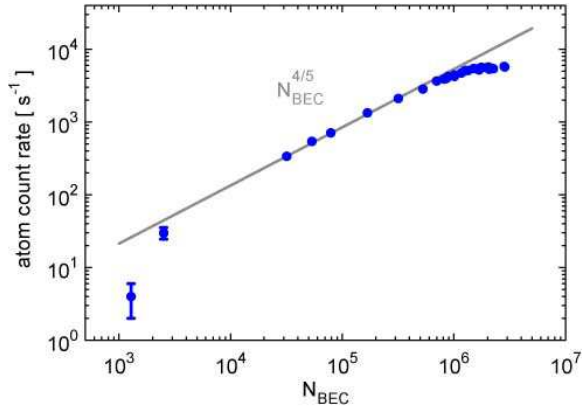


Figure 18: Investigation of detected atom count rates for pure quantum degenerate samples. The scaling with the atom number in a pure BEC exhibits three different regimes. The expected $N_{\text{BEC}}^{4/5}$ behavior is only valid for intermediate particle numbers. Very small and very large condensates obey different scaling laws due to an increased Heisenberg limited momentum spread and the mean field repulsion of the remaining condensate, respectively.

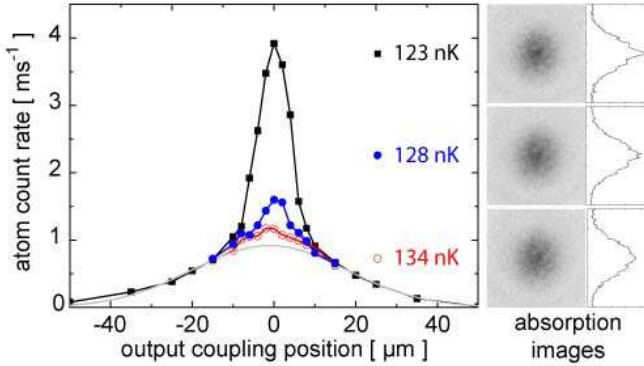


Figure 19: Analysis of the density distribution of the trapped ultracold atom gas by output coupling at different vertical positions relative to the center of the BEC and measuring the resulting atom count rate with the cavity. The profiles for three different temperatures around T_c are shown in comparison with the absorption images. The high sensitivity of the cavity detector to quantum degenerate atoms allows for precise observation of the onset of Bose-Einstein condensation and the deviations from a Gaussian profile (gray curve).

Furthermore we are able to survey the density distribution in the trap along the vertical direction by scanning the resonant plane for the output coupling process through the trapped cloud of cold atoms (Fig. 19). For temperatures close to the critical temperature the density distribution of the thermal cloud already deviates from the Gaussian shape and has to be described by the more peaked Bose distribution [Fig. 19, 134 nK]. For temperatures slightly below T_c single atom detection with the cavity allows us to observe and map very small condensates that are not visible in absorption images [Fig. 19, 128 nK and 123 nK]. This could be a valuable tool to

study the temporal and spatial evolution of the bosonic gas at the phase transition.

VIII. DISCUSSION

We have presented an apparatus that achieves the fusion of BEC production with the single atom detection ability in the strong coupling regime of cavity QED. The challenge to experimentally merge these two fields was overcome by forging new paths for the Bose-Einstein condensation setup and the ultrahigh finesse optical cavity design.

The concept of the experimental realization is based on intertwined technological modules: A nested vacuum system design with an internal higher background pressure MOT chamber, an *in vacuo* magnetic transport arrangement cooled to -90°C and the modular, exchangeable science platform providing access for samples and probes to the Bose-Einstein condensate. The system is distinguished by very reliable and reproducible operation for the production of large Bose-Einstein condensates and stable, continuous atom lasers. It features flexibility for research and applications of atom lasers through the vast, free and accessible half-space below the BEC.

In particular, we have implemented on the science platform a very compact realization of an ultrahigh finesse optical cavity design including a proper, UHV compatible vibration isolation system. With this experimental setup we are able to detect single atoms from a quantum degenerate source with high efficiency by aiming the atom laser into the cavity mode. The atom laser allows for a very high rate and controllable delivery of atoms into the cavity mode, which facilitates research of cavity QED in the strong coupling regime with single atoms. Moreover, the cavity as a single atom detector opens up the field of quantum atom optics and is especially useful to probe cold atomic clouds, particularly near the phase transition, nondestructively *in situ* and time resolved. Furthermore it is an extremely sensitive tool to detect atomic beams for high precision interferometry measurements and to investigate particle correlations.¹⁷

Future prospects with the system include single molecule detection and the setup of a heterodyne detection technique⁸⁵ for probing the presence of an atom inside the cavity mode which could be nondestructive on the atomic quantum state. Furthermore, we intend to transport the Bose-Einstein condensate into the ultrahigh finesse optical cavity. In the vertical direction we can apply a moving optical standing wave formed by a far red detuned dipole laser into which we could load the BEC and convey it downwards into the cavity. The arrangement of coils around the cavity can be used to apply magnetic field gradients for tomography experiments. The lateral optical access enables us to create three-dimensional optical lattices inside the ultrahigh finesse optical cavity which will open the route to study strongly correlated systems with single atom resolution.

Acknowledgments

We would like to thank Jean-Pierre Stucki, the mechanical workshop of the ETH Physics Department, Thilo Stöferle and Alexander C. Frank for aid in the construction and commissioning of the apparatus, and Thomas Bourdel and Tobias Donner for experimental as-

sistance and valuable discussions. We acknowledge funding by SEP Information Sciences, OLAQUI (EU FP6-511057), Quedis (ESF), and QSIT. Mention of industrial brand names is for technical communication only and does not constitute an endorsement of such products.

-
- * Electronic address: koehl@phys.ethz.ch
- ¹ C. J. Pethick and H. Smith, *Bose-Einstein Condensation in Dilute Gases* (Cambridge University Press, 2002).
 - ² *Cavity Quantum Electrodynamics*, in *Advances in Atomic, Molecular, and Optical Physics*, Suppl. 2, edited by P. R. Berman (Academic Press, 1994).
 - ³ M. H. Anderson, J. R. Ensher, M. R. Matthews, C. E. Wieman, and E. A. Cornell, *Science* **269**, 198 (1995).
 - ⁴ K. B. Davis, M.-O. Mewes, M. R. Andrews, N. J. van Druten, D. S. Durfee, D. M. Kurn, and W. Ketterle, *Phys. Rev. Lett.* **75**, 3969 (1995).
 - ⁵ M. R. Andrews, C. G. Townsend, H.-J. Miesner, D. S. Durfee, D. M. Kurn, and W. Ketterle, *Science* **275**, 637 (1997).
 - ⁶ M. R. Matthews, B. P. Anderson, P. C. Haljan, D. S. Hall, C. E. Wieman, and E. A. Cornell, *Phys. Rev. Lett.* **83**, 2498 (1999).
 - ⁷ C. Raman, M. Köhl, R. Onofrio, D. S. Durfee, C. E. Kulewicz, Z. Hadzibabic, and W. Ketterle, *Phys. Rev. Lett.* **83**, 2502 (1999).
 - ⁸ M.-O. Mewes, M. R. Andrews, D. M. Kurn, D. S. Durfee, C. G. Townsend, and W. Ketterle, *Phys. Rev. Lett.* **78**, 582 (1997).
 - ⁹ B. P. Anderson and M. A. Kasevich, *Science* **282**, 1686 (1998).
 - ¹⁰ E. W. Hagley, L. Deng, M. Kozuma, J. Wen, K. Helmerston, S. L. Rolston, and W. D. Phillips, *Science* **283**, 1706 (1999).
 - ¹¹ I. Bloch, T. W. Hänsch, and T. Esslinger, *Phys. Rev. Lett.* **82**, 3008 (1999).
 - ¹² M. Greiner, O. Mandel, T. Esslinger, T. W. Hänsch, and I. Bloch, *Nature (London)* **415**, 39 (2002).
 - ¹³ T. Stöferle, H. Moritz, C. Schori, M. Köhl, and T. Esslinger, *Phys. Rev. Lett.* **92**, 130403 (2004).
 - ¹⁴ S. Inouye, M. R. Andrews, J. Stenger, H.-J. Miesner, D. M. Stamper Kurn, and W. Ketterle, *Nature (London)* **392**, 151 (1998).
 - ¹⁵ E. A. Donley, N. R. Claussen, S. L. Cornish, J. L. Roberts, E. A. Cornell, and C. E. Wieman, *Nature (London)* **412**, 295 (2001).
 - ¹⁶ S. Fölling, F. Gerbier, A. Widera, O. Mandel, T. Gericke, and I. Bloch, *Nature (London)* **434**, 481 (2005).
 - ¹⁷ A. Öttl, S. Ritter, M. Köhl, and T. Esslinger, *Phys. Rev. Lett.* **95**, 090404 (2005).
 - ¹⁸ M. Schellekens, R. Hoppeler, A. Perrin, J. V. Gomes, D. Boiron, A. Aspect, and C. I. Westbrook, *Science* **310**, 648 (2005).
 - ¹⁹ R. J. Thompson, G. Rempe, and H. J. Kimble, *Phys. Rev. Lett.* **68**, 1132 (1992).
 - ²⁰ H. Mabuchi, Q. A. Turchette, M. S. Chapman, and H. J. Kimble, *Opt. Lett.* **21**, 1393 (1996).
 - ²¹ P. Münstermann, T. Fischer, P. Maunz, P. W. H. Pinkse, and G. Rempe, *Phys. Rev. Lett.* **82**, 3791 (1999).
 - ²² C. J. Hood, T. W. Lynn, A. C. Doherty, A. S. Parkins, and H. J. Kimble, *Science* **287**, 1447 (2000).
 - ²³ J. Ye, D. W. Vernooy, and H. J. Kimble, *Phys. Rev. Lett.* **83**, 4987 (1999).
 - ²⁴ P. W. H. Pinkse, T. Fischer, P. Maunz, and G. Rempe, *Nature (London)* **404**, 365 (2000).
 - ²⁵ S. J. van Enk, J. McKeever, H. J. Kimble, and J. Ye, *Phys. Rev. A* **64**, 013407 (2001).
 - ²⁶ P. Maunz, T. Puppe, I. Schuster, N. Syassen, P. W. H. Pinkse, and G. Rempe, *Nature (London)* **428**, 50 (2004).
 - ²⁷ A. Kuhn, M. Hennrich, and G. Rempe, *Phys. Rev. Lett.* **89**, 067901 (2002).
 - ²⁸ J. McKeever, A. Boca, A. D. Boozer, R. Miller, J. R. Buck, A. Kuzmich, and H. J. Kimble, *Science* **303**, 1992 (2004).
 - ²⁹ J. I. Cirac, P. Zoller, H. J. Kimble, and H. Mabuchi, *Phys. Rev. Lett.* **78**, 3221 (1997).
 - ³⁰ M. G. Moore and P. Meystre, *Phys. Rev. Lett.* **85**, 5026 (2000).
 - ³¹ D. Jaksch, S. A. Gardiner, K. Schulze, J. I. Cirac, and P. Zoller, *Phys. Rev. Lett.* **86**, 4733 (2001).
 - ³² C. Maschler and H. Ritsch, *Phys. Rev. Lett.* **95**, 260401 (2005).
 - ³³ T. Bourdel, T. Donner, S. Ritter, A. Öttl, M. Köhl, and T. Esslinger, *Phys. Rev. A* **73**, 043602 (2006).
 - ³⁴ P. Bouyer and M. A. Kasevich, *Phys. Rev. A* **56**, R1083 (1997).
 - ³⁵ P. Horak, B. G. Klappauf, A. Haase, R. Folman, J. Schmiedmayer, P. Domokos, and E. A. Hinds, *Phys. Rev. A* **67**, 043806 (2003).
 - ³⁶ S. Eriksson, M. Trupke, H. Powell, D. Sahagun, C. Sinclair, E. Curtis, B. Sauer, E. Hinds, Z. Moktadir, C. Golasch, et al., *Eur. Phys. J. D* **35**, 135 (2005).
 - ³⁷ M. Greiner, I. Bloch, T. W. Hänsch, and T. Esslinger, *Phys. Rev. A* **63**, 031401 (2001).
 - ³⁸ H. J. Lewandowski, D. M. Harber, D. L. Whitaker, and E. A. Cornell, *J. Low Temp. Phys.* **132**, 309 (2003).
 - ³⁹ C. Wieman, G. Flowers, and S. Gilbert, *Am. J. Phys.* **63**, 317 (1995).
 - ⁴⁰ J. Fortagh, A. Grossmann, T. W. Hänsch, and C. Zimmermann, *J. Appl. Phys.* **84**, 6499 (1998).
 - ⁴¹ *CERN Accelerator School: Vacuum Technology*, edited by S. Turner (CERN, 1999).
 - ⁴² http://en.wikipedia.org/wiki/Stainless_steel.
 - ⁴³ thermally conductive epoxy, Emerson & Cuming.
 - ⁴⁴ thermally durable, low outgassing polyimide, DuPont.
 - ⁴⁵ low outgassing fluoroelastomer, DuPont.
 - ⁴⁶ machineable tungsten heavy alloy, M & I Materials.
 - ⁴⁷ low outgassing fluoropolymer, DuPont.

- ⁴⁸ low outgassing, machineable polyimide, DuPont.
- ⁴⁹ low outgassing, machinable glass ceramic, Corning.
- ⁵⁰ thermally conductive, low outgassing, machinable high strength ceramic (AlN), Precision Ceramics.
- ⁵¹ J. M. Laurent and G. Losch, CERN, *Bake-out Procedure for Lab Work* (1997), private communication.
- ⁵² T. Esslinger, I. Bloch, and T. W. Hänsch, Phys. Rev. A **58**, R2664 (1998).
- ⁵³ RC311, FTS Systems.
- ⁵⁴ T. Bergeman, G. Erez, and H. J. Metcalf, Phys. Rev. A **35**, 1535 (1987).
- ⁵⁵ HP 6683A, Agilent.
- ⁵⁶ BCS 15/10, HighFinesse.
- ⁵⁷ Vakuumschmelze
- ⁵⁸ A. Marte, T. Volz, J. Schuster, S. Dürr, G. Rempe, E. G. M. van Kempen, and B. J. Verhaar, Phys. Rev. Lett. **89**, 283202 (2002).
- ⁵⁹ SiO₂/TiO₂ on BK7, $\mathcal{T} < 4 \times 10^{-6}$, $\mathcal{S} < 10 \times 10^{-6}$ (“best effort”), Research Electro-Optics.
- ⁶⁰ P. Münstermann, T. Fischer, P. Pinkse, and G. Rempe, Opt. Commun. **159**, 6367 (1999).
- ⁶¹ BM532, Sortech.
- ⁶² *Shock and Vibration Handbook*, edited by C. M. Harris and A. G. Piersol (McGraw-Hill, 2002).
- ⁶³ C. Gerber, G. Binnig, H. Fuchs, O. Marti, and H. Rohrer, Rev. Sci. Instrum. **57**, 221 (1986).
- ⁶⁴ M. Okano, K. Kajimura, S. Wakiyama, F. Sakai, W. Mizutani, and M. Ono, J. Vac. Sci. Technol. A **5**, 3313 (1987).
- ⁶⁵ A. I. Oliva, Victor Sosa, R. de Coss, Raquel Sosa, N. Lopez Salazar, and J. L. Pena, Rev. Sci. Instrum. **63**, 3326 (1992).
- ⁶⁶ A. I. Oliva, M. Aguilar, and Víctor Sosa, Meas. Sci. Technol. **9**, 383 (1998).
- ⁶⁷ digital card: DIO-64, Viewpoint Systems.
analog cards: PCI6713 & PCI6733, National Instruments.
- ⁶⁸ W. Ketterle, D. S. Durfee, and D. M. Stamper Kurn, in *Bose-Einstein Condensation in Atomic Gases*, Proceedings of the International School of Physics Enrico Fermi vol. CXL edited by M. Inguscio, S. Stringari, and C. Wieman, (IOS Press, Amsterdam, 1999), pp. 67–176.
- ⁶⁹ U. Schünemann, H. Engler, R. Grimm, M. Weidemüller, and M. Zielonkowski, Rev. Sci. Instrum. **70**, 242 (1999).
- ⁷⁰ L. Ricci, M. Weidemüller, T. Esslinger, A. Hemmerich, C. Zimmermann, V. Vuletic, W. König, and T. W. Hänsch, Opt. Commun. **117**, 541 (1995).
- ⁷¹ G. C. Bjorklund, M. D. Levenson, W. Lenth, and C. Ortiz, Appl. Phys. B **32**, 145 (1983).
- ⁷² Alta E1, Apogee.
- ⁷³ R. J. Glauber, Phys. Rev. **130**, 2529 (1963).
- ⁷⁴ D. A. Steck, *Rubidium 87 D Line Data* (2001), <http://steck.us/alkalidata>.
- ⁷⁵ N. P. Robins, A. K. Morrison, J. J. Hope, and J. D. Close, Phys. Rev. A **72**, 031606 (2005).
- ⁷⁶ HP 83712A, Agilent.
- ⁷⁷ R. Graham and D. F. Walls, Phys. Rev. A **60**, 1429 (1999).
- ⁷⁸ H. Steck, M. Naraschewski, and H. Wallis, Phys. Rev. Lett. **80**, 1 (1998).
- ⁷⁹ Y. B. Band, P. S. Julienne, and M. Trippenbach, Phys. Rev. A **59**, 3823 (1999).
- ⁸⁰ R. Ballagh and C. M. Savage, Mod. Phys. Lett. B **14 Suppl.**, 153 (2000).
- ⁸¹ J. Schneider and A. Schenzle, Appl. Phys. B **69**, 353 (1999).
- ⁸² C. J. Lee, Phys. Rev. A **61**, 063604 (2000).
- ⁸³ V. I. Balykin and V. S. Letokhov, Opt. Commun. **64**, 151 (1987).
- ⁸⁴ R. B. Doak, R. E. Grisenti, S. Rehbein, G. Schmahl, J. P. Toennies, and C. Woll, Phys. Rev. Lett. **83**, 4229 (1999).
- ⁸⁵ H. Mabuchi, J. Ye, and H. Kimble, Appl. Phys. B **68**, 1095 (1999).
- ⁸⁶ R. W. P. Drever, J. L. Hall, F. V. Kowalski, J. Hough, G. M. Ford, A. J. Munley, and H. Ward, Appl. Phys. B **31**, 97 (1983).
- ⁸⁷ M. Prevedelli, T. Freearde, and T. W. Hänsch, Appl. Phys. B **60**, S241 (1995).
- ⁸⁸ J. F. Kelly and A. Gallagher, Rev. Sci. Instrum. **58**, 563 (1987).
- ⁸⁹ E. Jaynes and F. Cummings, Proc. IEEE **51**, 89 (1963).
- ⁹⁰ B. W. Shore and P. L. Knight, J. Mod. Optics **40**, 1195 (1993).
- ⁹¹ SPCM-ARQ-15, PerkinElmer.
- ⁹² C. Salomon, J. Dalibard, A. Aspect, H. Metcalf, and C. Cohen Tannoudji, Phys. Rev. Lett. **59**, 1659 (1987).
- ⁹³ NS-5/V2, HL Planartechnik.
- ⁹⁴ P. Pinkse, T. Fischer, P. Maunz, T. Puppe, and G. Rempe, J. Mod. Opt. **47**, 2769 (2000).
- ⁹⁵ Y. Le Coq, J. H. Thywissen, S. A. Rangwala, F. Gerbier, S. Richard, G. Delannoy, P. Bouyer, and A. Aspect, Phys. Rev. Lett. **87**, 170403 (2001).
- ⁹⁶ M. Köhl, T. Busch, K. Mölmer, T. W. Hänsch, and T. Esslinger, Phys. Rev. A **72**, 063618 (2005).
- ⁹⁷ S. Seidelin, J. Viana Gomes, R. Hoppeler, O. Sirjean, D. Boiron, A. Aspect, and C. I. Westbrook, Phys. Rev. Lett. **93**, 090409 (2004).
- ⁹⁸ A. S. Tychkov, T. Jelte, J. M. McNamara, P. J. J. Tol, N. Herschbach, W. Hogervorst, and W. Vassen, Phys. Rev. A **73**, 031603 (2006).
- ⁹⁹ J.-F. Riou, W. Guerin, Y. Le Coq, M. Fauquembergue, P. Bouyer, V. Josse, and A. Aspect, cond-mat/0509281.
- ¹⁰⁰ Vakuumschmelze